WAVE FIELD SYNTHESIS ACOUSTICS, ELECTROMAGNETICS AND LC LATTICES

A Dissertation

Presented to the Faculty of the Graduate School

of Cornell University

in Partial Fulfillment of the Requirements for the Degree of

Doctor of Philosophy

by

Georgios Nektarios Lilis

January 2009

WAVE FIELD SYNTHESIS

ACOUSTICS, ELECTROMAGNETICS

AND LC LATTICES

Georgios Nektarios Lilis, Ph.D.

Cornell University 2009

By calculating accurately the signals of wave sources following specific techniques, one can use their induced wave fields, in order to synthesize wave patterns with predefined spatial and temporal characteristics, inside various wave media.

Using the previous idea, the first part of this thesis presents a linear wave field synthesis method which has potential applications in acoustic and electromagnetic media. Virtual sound reproduction mechanisms used in theaters and teleconference systems, as well as medical devices using ultrasound and electromagnetic radiation, could benefit from this method. The method is compared with traditional acoustic wave field synthesis techniques and simulations demonstrating its applicability on different source topologies with different radiation characteristics are also presented.

Unlike the linear analysis of the first part, the second part of this thesis is focused on the theoretical and experimental study of certain nonlinear wave field synthesis phenomena which appear on two dimensional nonlinear LC lattices. More specifically, it is demonstrated how nonlinearity can help in synthesizing high frequency and high power wave pulses at the central points of these lattices, using many low power and low frequency sources at the boundaries. This idea has potential applications in ultra wide band communication and imaging systems and holds a promise of ”closing the Terahertz window” formed by the power vs. frequency performance of electronic and optical devices.

BIOGRAPHICAL SKETCH

Georgios N. Lilis received his B.Sc. degree in Electrical Engineering from the National Technical University of Athens (N.T.U.A) in 2002. He worked for the Antenna Laboratory of N.T.U.A implementing RF switching on compound antenna modules. Georgios joined Cornell Communications Networks Research (CCNR) group in 2004, where he studied acoustic implementations of Wave Field Synthesis. He received his M.S. degree in Electrical Engineering from Cornell University in 2006. In 2007 he joined the Ultra-wide band Nonlinear Integrated Circuits (UNIC) Lab in Cornell University where he studied the electromagnetic wave field synthesis observed in nonlinear LC electrical lattices. His research interests span the general area of wave propagation phenomena in various media, with a focus on acoustic and electromagnetic implementations.

The greatest enemy of evil is humility.
We have to treat all others as saints and ourselves as sinners and inferior of all.
Although others could be sinners,
we do not have the right to judge and treat them as sinners.

If the evil brings us disturbing thoughts in our intellectual work different from the ones leading to the salvation of our souls we have to fight them with the internal prayer.

Ask for repentance in your prayer and nothing else, neither for divine lights, nor miracles, nor prophecies, nor spiritual gifts, nothing but repentance. Repentance will bring you humility. Humility will bring you the Grace of God. God will have in his grace everything you need for your salvation or anything you might need to help another soul.

Let your soul be thirsty for the knowledge of the truth, the forgiveness of the sins, the peace of mind, the heavenly joy... Let your soul wait for the time when it will be released from the vanity of the present world, the pain, the sorrow, the evil which exists in the hearts of people.

Monk Paisios

ACKNOWLEDGEMENTS

I would like to acknowledge my two advisers, professor Sergio Servetto and professor Ehsan Afshari, who spent countless hours discussing and helping me in various topics related with the present thesis. I would like to thank professor Subrata Mukherjee and professor Nicholas Zabaras for their advice on numerical techniques and professor Leonard Gross for his suggestions on math related aspects of this work. I would like also to express my thanks to professor Clifford Pollock, professor Sunil Bhave, professor Terrence Fine, professor Stephen Wicker and professor Andrea Goldsmith for their support after the unexpected loss of professor Servetto. Without their help, this work would not have been realized at all.

Also I would like to thank Master's student Jihyuk Park for his help during the construction and the measurements of the LC lattice and Ph.D. student Omeed Momeni for his useful suggestions on circuit related topics.

TABLE OF CONTENTS

LIST OF TABLES

LIST OF FIGURES

CHAPTER 1

INTRODUCTION

1.1 Wave Field Synthesis

Wave propagation is a subject of study in many scientific fields, such as acoustics, geophysics, electro-magnetics and optics [1, 4, 2, 3]. In these areas, there is an increased interest in finding systematic methods of synthesizing wave fields with certain spatial and temporal characteristics. This concept of wave field synthesis (WFS) is built upon the ability to generate wave patterns using spatially distributed wave sources. The goal of WFS is to determine the signals such that, when applied to the distributed wave sources, their induced individual fields, synthesize a given desirable wave field.

A fundamental requirement for WFS experiments is the existence of a wave medium. Such medium could be any material inside which waves can propagate without significant absorption. Examples include acoustic and electromagnetic media, as well as electrical LC lattices where electromagnetic wave propagation can be generated under certain conditions.

Apart from the existence of the wave medium equally important is a mechanism called wave source capable of generating wave patterns inside the medium. In the case of acoustics, a source could be a loudspeaker or a music instrument, in the case of electromagnetics a current dipole and in the case of electrical lattices, a voltage source. The carefully designed cumulative action of many of such sources inside the medium results to the accurate synthesis of desirable wave patterns.

1.2 Organization

Based of the nature of the wave medium this thesis is divided into three chapters. The first chapter discusses WFS principles applied in acoustic media with applications in multichannel sound reproduction systems. Acoustic wave fields are simple scalar wave fields which represent atmospheric pressure variations.

Unlike acoustic fields, electromagnetic fields are vector fields which are generally more complex. In spite of this inherent complexity, the proposed method used for the synthesis of scalar acoustic fields can be generalized to the synthesis electromagnetic vector fields. As a consequence, electromagnetic wave field synthesis with applications in antenna arrays is discussed in the second chapter.

In the first two chapters the wave medium is assumed to be linear meaning that the wave field induced by many wave sources is the same as the sum of the wave fields induced by each source individually. This assumption does not hold for nonlinear wave media such as nonlinear LC lattices. These lattices allow electromagnetic waves to propagate in a nonlinear manner. By applying voltage sources in the boundary nodes of these lattices nonlinear electromagnetic wave field synthesis phenomena can be observed in their central nodes. Under certain optimal conditions, and due to the nonlinear nature of the wave medium, the input signals of the boundary source nodes can be amplified significantly in the center of the lattice. This phenomenon is studied in the third and final chapters. Experimental results consisting of voltage measurements on a real LC lattice are also presented.

1.3 Notation

Relevant notations that are used throughout the thesis are listed below:

$\hat{P}(\vec{r}, \omega)$ acoustic pressure variation spectrum at location $\vec{r}$ and frequency ω.

$\hat{S}_j(\omega)$ is the complex spectral value of source source j at frequency ω.

$\{x_n\}$ represents vector x_n.

$\{\hat{x}_n\}$ represents the fourier transform of vector x_n.

$\{x_n\}_q$ represents the q^{th} element of vector x_n.

$\{x(\omega)\}$ represents a vector x of functions of ω.

$[X_n]$ represents matrix X_n.

$[X_n]_{pq}$ represents the pq^{th} element of matrix X_n.

$[X(\omega)]$ represents a matrix X of functions of ω.

$\{x\}.\{y\} = \{x_1 y_1, ..., x_N y_N\}$ is the element by element multiplication.

$\{x\} * \{y\} = \{x_1 * y_1, ..., x_N * y_N\}$ is the element by element convolution.

$\{x_{k:m}\} = \{x_k, x_k + 1, ..., x_m\}$ part of $\{x\}$ vector from k to m element ($m > k$).

$0_{N \times N}$ matrix of zeros with dimensions $N \times N$.

0_k vector containing k zeros.

CHAPTER 2

ACOUSTICS

2.1 Wave Field Synthesis in Acoustics

In room acoustics WFS can be used to generate a good replica of the sound field of an instrument, using a distributed array of loudspeakers. This idea has excellent applications in theaters and cinemas, as a sound enhancement technique [5] and in home-theaters, simulators and teleconference systems, as a spatial sound reproduction mechanism [6]. Recently, applications of this concept in electronic music have also been proposed [7].

Figure 2.1 displays an application of WFS in acoustics. An important requirement in every sound field synthesis experiment is the existence of a unit capable of sending electrical signals to the acoustic sources called control center (refer to Fig. 2.1).

The idea of synthesizing ultrasound wave fields inside biological media appears also in cancer treatment applications and more specifically in a method called hyperthermia. Using a number of distributed ultrasound sources [8, 9] outside the human body, a focused ultrasound field can be synthesized inside the body. This focused ultrasound field

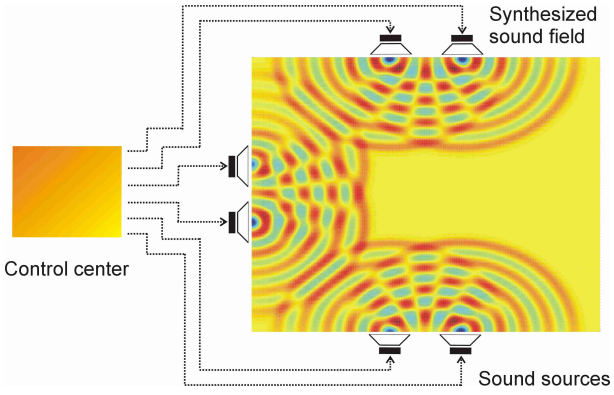

Figure 2.1: WFS in acoustics

can overheat the tumor region and kill the cancer cells. In order to achieve optimal focusing a space-time inverse filtering process has been introduced [10].

2.1.1 Challenges

Intuition suggests that the greater the number of wave sources, the better the quality of the synthesis. However, difficulties in implementation arise when the number of sources is too large, and the communications between the sources and the control center is established through wires. A reasonable solution in such cases is to replace the wired links, as shown in Figure 2.1, with wireless links. Inevitably, any communication impairment between the control center and wave sources affects the quality of the synthesized field. For example, in a wireless setting any synchronization inability or noise added to the wave source signals causes additional error accumulation between the desirable and the synthesized wave fields. The need of a synchronous network infrastructure to support the WFS apparatus is also discussed in [13].

Medium heterogeneities impose another obstacle towards a successful wave field synthesis experiment. For example, the walls of a room scatter the incident waves, generating destructive interference to the synthesized fields. In order to cancel these scattering effects, many algorithms have been proposed by Spors [14] and by Gauthier *et al.*[15, 16] who introduced an adaptive WFS method. Temporal and spatial heterogeneities also appear in cancer treatment, when biological tissues are treated as a wave medium [17]. In such cases, spatial and temporal discretization of the wave medium and application of Finite Element Methods [18] have been suggested [19]. In all of the above scenarios an optimal wave field synthesis method appears to be desirable.

2.1.2 Historical overview

An early investigation of the methods of synthesizing sound fields was conducted by M.Camras in 1968 [20]. Following similar ideas A. J. Berkhout introduced an acoustic holography method in 1988 [21] and defined formally WFS in 1993 [22, 23]. The WFS method defined by Berkhout, is based on a principle discovered by a Dutch physicist, Christian Huygens, in 1678. According to this principle, at any instant the wavefront of a propagating wave of light conforms to the envelope created by spherical wavelets emanating from every point of the wavefront at a prior instant [24]. Huygens' principle can be expressed using the Kirchhoff-Rayleigh integral equation [4], which states that a pressure field can be synthesized using distributed monopole or dipole wave sources with specific amplitudes. Following Berkhout's method, various research groups [25, 26, 28, 27], have studied acoustic WFS synthesis implementations. Effects of directionality in wave sources implementing WFS have also been studied [29].

Apart from acoustics, an iterative wave synthesis algorithm has been proposed by R.Piestun, B.Spektop and J.Shamir in optics [11, 12]. This method achieves the synthesis of three dimensional light wave fields and has applications in optical holography.

2.1.3 Main Contributions

This chapter introduces a spectral wave field synthesis technique different from the approach based on the Kirchhoff-Rayleigh integral equation followed by traditional WFS methods. As mentioned in [22], in a real scenario the source arrays used for the synthesis have finite a length and a finite number of sources and approximations of the Kirchhoff-Rayleigh integral equation must be applied, which result in truncation and aliasing effects to the synthesized fields. The proposed method overcomes these effects

since it is optimal in the total square error sense: given a source topology and a desirable wave field, it determines certain optimal source signals. When these signals are applied to the sources, an optimal wave field is induced. The total square error between the optimal wave field and the desirable wave field is the smallest possible.

Traditional WFS methods require the synthesis sources to be located on a surface [4] with a structured topology (e.g. a line, a circle, etc.). This constraint does not appear in the proposed method since it can be applied to any arbitrary source topology.

Finally, the proposed method is more general than traditional WFS methods, since it can accommodate not only dipole and monopole sources which traditional WFS methods use, but also sources with general radiation profiles.

2.1.4 Organization

The problem of WFS is introduced as an optimization problem in the subsection 2.2.2 of this chapter. A solution to this optimization problem is presented for the synthesis of band limited sound fields. The existence and uniqueness of this solution is proven for the cases in which the synthesis sources are located at distinct points.

A comparison between the proposed technique and traditional WFS techniques is presented in subsection 2.3.1. The performance measure of the comparison is the total square error between the desirable (target) and the synthesized fields. In all attempted synthesis scenarios, the proposed method has lower total square error than the total square error of traditional WFS techniques.

The feasibility of the proposed technique on an arbitrary source topology is investigated in subsection 2.3.2. In this scenario, the quality of synthesis is assessed using

energy contour plots.

Finally, the ability of the proposed method, in handling sources with different radiation profiles is illustrated in subsection 2.3.3.

2.2 Optimal wave field synthesis

2.2.1 Preliminaries

Synthesis Error

In order to perform a successful wave field synthesis experiment, appropriate signals have to be specified for the distributed wave sources. In many cases however, the locations of the wave sources become the main obstacle in accurately synthesizing a desirable wave field. Given any source topology, knowledge of the best possible field which can be synthesized is required. The term "best possible wave field" refers to the wave field that has the smallest possible difference with the desirable wave field.

Wave fields are usually scalar functions of space and time. Assume a time instant $t \in (-\infty, \infty)$ and a point represented by $\vec{r}$ inside a wave medium S. By means of functional analysis [31], one can define the difference d_{P_1,P_2} [1] between two wave field functions $P_1(\vec{r}, t)$ and $P_2(\vec{r}, t)$ inside S, as follows:

$$d_{P_1,P_2} = \|P_1 - P_2\|_2^2 = \int_S \left[\int_{-\infty}^{\infty} \left| P_1(\vec{r}, t) - P_2(\vec{r}, t) \right|^2 dt \right] d\vec{r} \tag{2.1}$$

[1] In functional analysis the difference d_{P_1,P_2} is defined as distance in vector spaces.

Generally, sound fields can be represented by the pressure variation fields $P(\vec{r}, t)$, which are scalar functions, and the difference expression (2.1) can be applied to them. Furthermore, using Parseval's theorem [31], one can pass from the time domain (t) to the frequency domain (ω), and express the differences between pressure variation fields as differences between pressure variation spectra:

$$d_{\hat{P}_1,\hat{P}_2} = \int_S \frac{1}{2\pi} \left[\int_{-\infty}^{\infty} \left| \hat{P}_1(\vec{r}, \omega) - \hat{P}_2(\vec{r}, \omega) \right|^2 d\omega \right] d\vec{r} \tag{2.2}$$

In a wave field synthesis experiment, the difference between the target spectral field ($\hat{P}_o(\vec{r}, \omega) = \hat{P}_1(\vec{r}, \omega)$), and the synthesized spectral field using finite distributed wave sources ($\hat{P}_s(\vec{r}, \omega) = \hat{P}_2(\vec{r}, \omega)$), is defined as the synthesis error E:

$$E = 2\pi d_{\hat{P}_o,\hat{P}_s} = \int_S \left[\int_{-\infty}^{\infty} \left| \hat{P}_o(\vec{r}, \omega) - \hat{P}_s(\vec{r}, \omega) \right|^2 d\omega \right] d\vec{r} \tag{2.3}$$

2.2.2 Optimal Wave Field Synthesis using point sources

Synthesis error as a function of the source spectra

Consider the problem of synthesizing a spectral field $\hat{P}_o(\vec{r}, \omega)$ by M distributed point sources at fixed known locations $\vec{r}_j$ inside a medium S, with spectra $\hat{S}_j(\omega)$, $j_=1, ..., M$. These distributed sources will synthesize an acoustic field spectrum $\hat{P}_s(\vec{r}, \omega)$ which generally differs from the desirable field spectrum $\hat{P}_o(\vec{r}, \omega)$. If the sources are monopoles, they will synthesize a field that satisfy the Helmholtz wave PDE with $\hat{S}(\vec{r}, \omega) = \sum_{j=1}^{M} \hat{S}_j(\omega)\delta(\vec{r} - \vec{r}_j)$, according to [4], or:

$$\nabla^2 \hat{P}_s + \frac{\omega^2}{c^2} \hat{P}_s + \sum_{j=1}^{M} \hat{S}_j(\omega) \delta(\vec{r} - \vec{r}_j) = 0 \tag{2.4}$$

Using Green's function notation, it can be shown that the solution of the above PDE, assuming Sommerfeld conditions [32] at $|\vec{r}| \to \infty$, becomes:

$$\hat{P}_s(\vec{r}, \omega) = \sum_{j=1}^{M} \begin{cases} \hat{S}_j(\omega) G_j(\vec{r}, \omega) & \omega > 0 \\ 0 & \omega = 0 \\ \hat{S}_j^*(-\omega) G_j^*(\vec{r}, \omega) & \omega < 0 \end{cases} \qquad G_j(\vec{r}, \omega) = \frac{e^{-j\frac{\omega}{c}|\vec{r} - \vec{r}_j|}}{4\pi |\vec{r} - \vec{r}_j|} \tag{2.5}$$

In the case where distributed sources are not monopoles, the functions $G_j(\vec{r}, \omega)$ are replaced by appropriate ones that capture the radiation characteristics of the sources. Substituting (3.3) into (3.2) and taking into account that all the spectral functions are real functions ($S_j(-\omega) = S_j^*(\omega), G_j(\vec{r}, -\omega) = G_j^*(\vec{r}, \omega), \hat{P}_o(\vec{r}, -\omega) = \hat{P}_o^*(\vec{r}, \omega), \omega > 0$), the synthesis error can be expressed as a function of the source spectra of the distributed sources ($\{\hat{S}(\omega)\} = \{\hat{S}_1(\omega), ..., \hat{S}_M(\omega)\}$):

$$E(\{\hat{S}(\omega)\}) = 2 \int_S \left[\int_{\omega > 0} \left| \hat{P}_o(\vec{r}, \omega) - \sum_{j=1}^{M} \hat{S}_j(\omega) G_j(\vec{r}, \omega) \right|^2 d\omega \right] ds \tag{2.6}$$

Definition of optimal WFS

Based on (2.6) one can define the optimal point WFS problem as follows:

Given:

1. A wave medium S,
2. M distributed sources at locations $\vec{r}_j \in S\,(j = 1, ..., M)$ and
3. A target field spectrum $\hat{P}_o(\vec{r}, \omega)$, $\vec{r} \in S$, $\omega \in \Omega \subset \mathcal{R}^+$.

Specify:

The optimal source spectra $\{\hat{S}^{opt}(\omega)\} = \{\hat{S}_1^{opt}(\omega), ..., \hat{S}_M^{opt}(\omega)\}$ from the set of square integrable complex functions with domain Ω (denoted by $\mathcal{L}^2[\Omega]$)[1], which minimize the synthesis error given by (2.6):

$$\{\hat{S}^{opt}(\omega)\} = \arg \min_{\hat{S}_j(\omega) \in \mathcal{L}^2[\Omega]} \left[E(\{\hat{S}(\omega)\}) \right] \tag{2.7}$$

2.2.3 Solution in different spaces

At a first glance, solving directly the WFS optimization problem defined in section 2.2.2 for the class of square integrable spectra $\mathcal{L}^2[\Omega]$ appears to be a daunting task. Consequently, the solution can be found in simpler solution spaces. For this purpose, simpler spectral classes are defined and denoted by $\Sigma_n[\Omega]$ $(n \in N)$ [2], in which the band Ω is partitioned into a total of 2^n equal-length sub-bands.

[1] The class $\mathcal{L}^2[\Omega]$ is formally defined in section A.3.1 of appendix.
[2] The classes $\Sigma_n[\Omega]$ are formally defined in section A.1.1 of the Appendix.

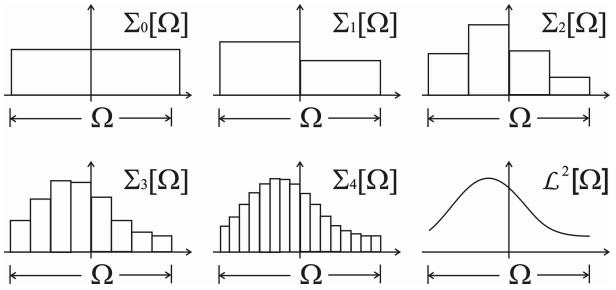

Figure 2.2: Representation of a bandlimited source spectrum in spectral classes $\Sigma_k[\Omega]$, $k = 0, 1, 2, 3, 4$ and $\mathcal{L}^2[\Omega]$

The spectra contained in each of these classes are piecewise constant at each subband. Fig. 2.2 illustrates how a bandlimited spectrum in $\mathcal{L}^2[\Omega]$ can be represented by spectra belonging to the classes $\Sigma_n[\Omega]$, $n = 0, 1, 2, 3, 4$.

The simplest among the classes $\Sigma_n[\Omega]$ is the class $\Sigma_o[\Omega]$ in which the source spectra $\hat{S}_j(\omega)$ ($j = 1, ..., M$), obtain a constant complex value in Ω. Based on this, the integral over Ω in the synthesis error expression (2.6) can be calculated explicitly. In this case, the WFS optimization problem becomes a convex optimization problem with solution which can be calculated by the following [3]:

$$
\begin{aligned}
&\{\hat{S}_0^{opt}\} = \arg \min_{\hat{S}_j(\omega)\in\Sigma_0[\Omega]} \left[E(\{\hat{S}(\omega)\})\right] \\
&\{\hat{S}_0^{opt}\} = \{\hat{S}_{01}^{opt}, ..., \hat{S}_{0M}^{opt}\} \\
&\{\hat{S}_0^{opt}\} = [H]^{-1}\{l\} \\
&[H] \in C^{M\times M}, \quad \{l\} \in C^{1\times M} \\
&[H]_{pq} = \int_S \left[\int_\Omega G_p(\vec{r},\omega) G_q^*(\vec{r},\omega) d\omega\right] ds, \qquad \{l\}_q = \int_S \left[\int_\Omega \hat{P}_o(\vec{r},\omega) G_q^*(\vec{r},\omega) d\omega\right] ds \\
&p, q \in \{1, ..., M\}
\end{aligned}
\tag{2.8}
$$

[3] Analytic proof in section A.22 of the Appendix.

The solution in (2.8) is valid for narrow bands Ω. In the case where Ω is relatively large, partition of Ω into sub-bands, must be applied and similar convex optimization problems have to be solved in each sub-band separately. By increasing the total of partitions 2^n ($n \in \mathcal{N}$), the solutions $\{\hat{S}_n^{opt}(\omega)\}$ ($n \in \mathcal{N}$) in the classes $\Sigma_n[\Omega]$ can be obtained.

As shown in sections A.2 and A.3.4 of the Appendix these solutions converge asymptotically to the $\mathcal{L}^2[\Omega]$ solution $\{\hat{S}^{opt}(\omega)\}$, given by:

$$
\begin{aligned}
&\lim_{n\to\infty}\{\hat{S}_n^{opt}(\omega)\} = \{\hat{S}^{opt}(\omega)\} \\
&\{\hat{S}^{opt}(\omega)\} = \arg\min_{\hat{S}_j(\omega)\in\mathcal{L}^2[\Omega]}\left[E(\{\hat{S}(\omega)\})\right] \\
&\{\hat{S}^{opt}(\omega)\} = [H(\omega)^{-1}]\{l(\omega)\} \\
&[H(\omega)]_{pq} = \int_S G_p(\vec{r},\omega)G_q^*(\vec{r},\omega)ds \qquad \{l(\omega)\}_q = \int_S \hat{P}_o(\vec{r},\omega)G_q^*(\vec{r},\omega)ds \\
&p,q \in \{1,...,M\}
\end{aligned}
\tag{2.9}
$$

Existence and Uniqueness of the solution

Equations (2.9) and (2.8) determine the optimal complex spectrum coefficients $\hat{S}_j^{opt}$ ($j = 1,...,M$), of the signals of the distributed point wave sources, which perform the synthesis. Essentially, the optimal coefficients in $\hat{S}_j^{opt}$ define the required amplitudes and phase shifts of the signals of these sources.

Generally, the coefficients $\hat{S}_j^{opt}$ are complex values that depend on the matrix $[H]$, which is equivalent to the cross correlation matrix of Green's functions centered at the point source locations. In this way, the source topology affects the matrix $[H]$. The coefficients $\hat{S}_j^{opt}$ depend also on the vector $\{l\}$, which in turn depends on the cross corre-

lation of the Green's functions of the distributed point sources, with the field spectrum $\hat{P}_o(\vec{r}, \omega)$.

As long as the wave sources are located at distinct spatial locations $\vec{r}_j$ ($j = 1, ..., M$), the invertibility of the matrix $[H(\omega)]$, as well as the existence and uniqueness of the solution given by (2.8) and (2.9), is guaranteed. This is because the matrix $[H(\omega)]$ is positive-definite and Hermitian [4].

However, there are cases in which the $[H(\omega)]^{-1}$ does not exist. Consider the case of two wave sources located at exactly the same point. Their contribution will be equivalent to the contribution of a single wave source whose amplitude is the sum of the amplitudes of the two sources. Since there are infinite ways of generating the same sum with two numbers, the number of optimal solutions (in the square error sense) of our problem is infinite.

Our intuition is correct provided that, if wave sources i and j are at the same position, the functions $G_i(\vec{r}, \omega)$ and $G_j(\vec{r}, \omega)$ will be identical. In this case, and according to (2.9), the columns $h_{,i} = [h_{1i}h_{2i}...h_{Ai}]$ and $h_{,j} = [h_{1j}h_{2j}...h_{Mj}]$ will be identical. Similarly, the rows $h_{i,} = [h_{i1}h_{i2}...h_{iM}]$ and $h_{j,} = [h_{j1}h_{j2}...h_{jM}]$ will be identical. This will render the matrix $[H]$ singular with rank at most $M - 1$. Such cases can be handled using singular value decomposition techniques, which provide a solution that has minimum length out of all solutions in the infinite solution space [33].

[4] Analytic proof in the section A.5 of appendix.

2.3 Simulations

2.3.1 Comparison with the state of the art

In this section, the proposed technique is compared with WFS techniques based on the Kirkhoff-Heltmoltz integral equations. As displayed in the left plot of Fig. 2.3, a linear source topology was chosen for this comparison. For all the simulations the wave speed was considered $c = 340$ m/sec, and the space unit 0.085 m.

The synthesis using the proposed method was performed by dipoles. The resultant synthesized field ($\hat{P}_s^{opt}(\vec{r},\omega)$), was calculated from equation (3.3), in which the spectra $\hat{S}_j(\omega)$ were replaced by the optimal $\Sigma_o[\Omega]$ spectra (specified in (2.8)), and the functions $G_j(\vec{r},\omega)$ with the dipole radiation functions. In other words, the synthesized by the proposed method wave field, can be calculated by:

$$\hat{P}_s^{opt}(\vec{r},\omega) = \sum_{j=1}^{M} \hat{S}_{0j}^{opt} G_j(\vec{r},\omega) \qquad G_j(\vec{r},\omega) = \frac{e^{-j\frac{\omega}{c}|\vec{r}-\vec{r}_j|}(1+j\frac{\omega}{c}|\vec{r}-\vec{r}_j|)}{4\pi|\vec{r}-\vec{r}_j|^2}\cos(\phi_j) \quad (2.10)$$

with $\vec{r}_j \in S$ the locations of the synthesis sources ($j = 1, ..., M$), and ϕ_j the angle formed by the vector $\vec{r}_j$ and the normal vector to the array surface at the point of the j^{th} source.

The field synthesized by the traditional WFS method ($\hat{P}_s^{WFS}(\vec{r},\omega)$) was calculated based on the approximation of Kirkhoff-Heltmoltz integral equation:

$$\hat{P}_s^{WFS}(\vec{r},\omega) = \sum_{j=1}^{M} \hat{P}_o(\vec{r}_j,\omega)\left(\frac{1+ik|\vec{r}-\vec{r}_j|}{2\pi|\vec{r}-\vec{r}_j|^2}\cos(\phi_j)\times e^{-jk|\vec{r}-\vec{r}_j|}\right)\Delta x\Delta y \quad (2.11)$$

where:

1. $\vec{r}_j \in S$ the locations of the synthesis sources $j = 1, ..., M$,
2. $P_o(\vec{r}_j, \omega)$ the sampled target wave field given by (2.13) at point source locations,
3. $\Delta x = \Delta y = 1$ unit the spatial occupancy of the point sources according to Figure 2.3 and
4. ϕ_j is the angle formed by the vector $\vec{r}_j$ and the normal to the array surface vector at the point of the j^{th} source.

The performance measure used to compare these two methods is the synthesis error defined in (3.2). By this definition, the synthesis error of the proposed technique, denoted as e^{opt}, and that of the traditional WFS method, denoted as e^{WFS}, referring to the frequency band Ω, can be calculated by:

$$e^{opt} = \left\| \hat{P}_s^{opt} - \hat{P}_o \right\|_2^2 = \frac{1}{2\pi} \int_S \left[\int_\Omega \left| \hat{P}_s^{opt}(\vec{r}, \omega) - \hat{P}_o(\vec{r}, \omega) \right|^2 d\omega \right] d\vec{r}$$
$$e^{WFS} = \left\| \hat{P}_s^{WFS} - \hat{P}_o \right\|_2^2 = \frac{1}{2\pi} \int_S \left[\int_\Omega \left| \hat{P}_s^{WFS}(\vec{r}, \omega) - \hat{P}_o(\vec{r}, \omega) \right|^2 d\omega \right] d\vec{r} \quad (2.12)$$

In all of the simulations the square medium S was defined by the following set of points: $S = \{(x, y, z) : \max(|x - 5|, |z - 5|) < 15, y = 0\}$. The narrow band $\Omega = [999Hz, 1001Hz]$ was selected to be the frequency range. In this band, the $\Sigma_o[\Omega]$ solution (2.8) is close to the $\mathcal{L}^2[\Omega]$ solution (2.9). The target wave field was chosen to be the wave field induced by a point source at $\vec{r}_o = (x_o, y_o, z_o) \in S$ (focal point), with flat spectrum equal to 1 $\forall \omega \in \Omega$. The spectral distribution of this wave field is given by:

$$\hat{P}_o(\vec{r}, \omega) = G_o(\vec{r}, \omega) = 1 \times \frac{e^{-j\frac{\omega}{c}|\vec{r} - \vec{r}_o|}}{4\pi|\vec{r} - \vec{r}_o|} \quad (2.13)$$

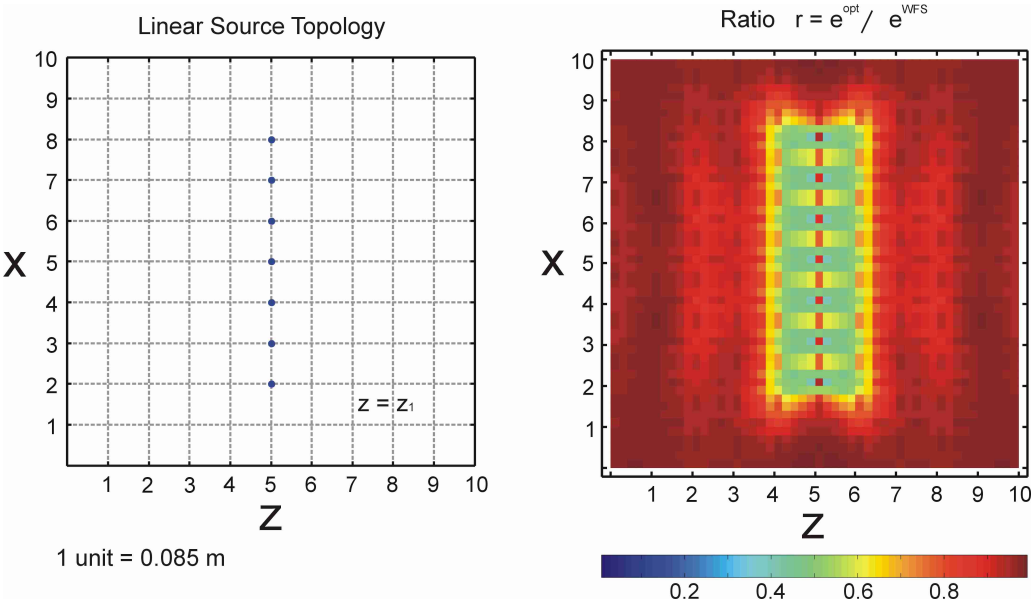

Figure 2.3: **Left:** Linear topology. **Right:** Distribution of the ratio values of the synthesis error induced by the proposed method over the synthesis error induced by traditional WFS, along the grid points.

We performed 2601 wave synthesis experiments. In each of these experiments, the location of the focal point of the target field was changed inside a two dimensional 51×51 orthogonal grid, defined by the following set of points:

$$\vec{r}_o = (0.2 * k, y_o, 0.2 * m) \;\; (k, m) \in \{0, ..., 50\} \times \{0, ..., 50\} \;\; y_o = 0 \tag{2.14}$$

For each one of the above grid points, we calculated the ratio of the resulting total error of the proposed technique over the total error of the traditional WFS technique, i.e., $r = e^{opt}/e^{WFS}$. The left plot of Fig. 2.3 display the spatial distribution of the calculated ratio values referring to all of the grid points.

Remarks

All of the obtained error ratios, displayed in the right plot of Fig. 2.3 are less than

1. This suggests that the performance of the proposed technique is better than the conventional WFS technique in all of the synthesis experiments. More specifically, when the focal point is close to the locations of the distributed sources (near field), the performance of the proposed method is superior. This can be justified by the truncation effects appearing in the traditional WFS technique, when the synthesized fields are focused near the source locations. These effects are caused by the finite number of synthesis sources. Furthermore, the performance of the traditional WFS technique converges asymptotically to the performance of the proposed method as the focal point of the target field moves far from the source locations.

2.3.2 Arbitrary source topologies

This section illustrates the applicability of the proposed technique on arbitrary source topologies. We considered a synthesis experiment in which the target field is induced by a point source at a point $\vec{r}_o = (5, 5)$, located at the center of a 10×10 square 2D region. As mentioned previously, the spectral distribution of the target field is given by (2.13) with $\vec{r}_o = (5, 5)$. In this scenario, the synthesis is accomplished by monopole point sources arbitrarily distributed in a 2D square region, as shown in the left plot of Fig. 2.4. The unit length, wave speed and frequency spectrum remained the same as in subsection 2.3.1 (1 unit =0.085 m, $c = 340$ m/sec, $\Omega = [999, 1001]$Hz). The $\Sigma_o[\Omega]$ synthesis solution (2.8) was considered here again.

In order to evaluate the quality of the synthesized field, its energy distribution is compared with that of the target field. These distributions are obtained from the following expressions:

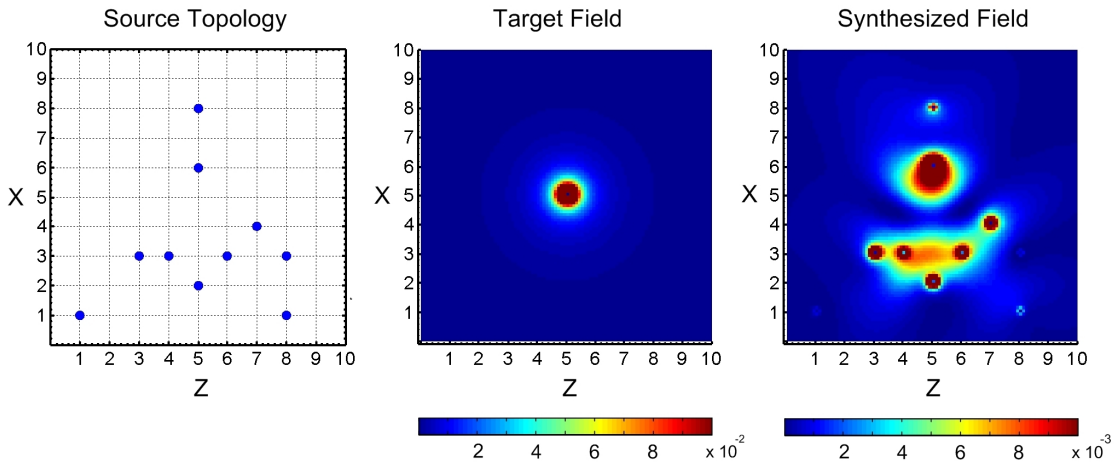

Figure 2.4: Optimal wave field synthesis by an arbitrary source topology. **Left:** Source Topology. **Center:** Energy distribution of the target field. **Right:** Energy distribution of the synthesized field

$$E_o(\vec{r}) = \frac{1}{2\pi}\int_{\Omega} \left|P_o(\vec{r},\omega)\right|^2 d\omega \qquad E_s(\vec{r}) = \frac{1}{2\pi}\int_{\Omega} \left|P_s(\vec{r},\omega)\right|^2 d\omega \qquad (2.15)$$

The energy distributions of the target and the synthesized fields, referring to the examined arbitrary source topology, are displayed in the center and right plots of Fig. 2.4 respectively.

Remarks

The proposed method optimally allocates the right amount of power to each source depending on its location with respect to the focal point $\vec{r}_o$. Greater power is allocated to sources closer to the focal point. As a result, the synthesized field emulates spatially the target field in the minimum total square error sense.

2.3.3 Optimal synthesis using directional point wave sources

Synthesis implementations using sources with different radiation characteristics can also be accommodated by the proposed method. The only required change is to replace the omnidirectional terms given by the Green's functions $G_j(\vec{r},\omega)$ with functions $D_j(\vec{r},\omega)$, describing the directional characteristics of the synthesizing sources. The rest of the analysis remains the same.

In order to illustrate this implementation, dipole and monopole point sources are included in the synthesis procedure. Two types of dipoles were considered with radiation characteristics described by the following spectral distributions:

$$D_j^A(\vec{r},\omega) = 1 \times \frac{e^{-j\frac{\omega}{c}|\vec{r}-\vec{r}_o|}(L * \cos\sqrt{|\phi|})(1+j\frac{\omega}{c}|\vec{r}-\vec{r}_o|)}{4\pi|\vec{r}-\vec{r}_o|^2}$$
$$D_j^B(\vec{r},\omega) = 1 \times \frac{e^{-j\frac{\omega}{c}|\vec{r}-\vec{r}_o|}(L * \cos\phi)(1+j\frac{\omega}{c}|\vec{r}-\vec{r}_o|)}{4\pi|\vec{r}-\vec{r}_o|^2}, \tag{2.16}$$

where L is the length of the dipole which is considered one space unit. The angle ϕ represents the azimuth angle measured from the center of the dipole.

A mixed monopole/dipole source topology displayed in the left plot of Fig. 2.5 was considered. The space unit, wave speed and spectrum remained the same as in subsections 2.3.1 and 2.3.2 (1 unit=0.085 m, $c = 340$ m/sec and $\Omega = [999, 1001]$Hz). Similarly, the $\Sigma_o[\Omega]$ solution from equation (2.8) was used here again. For simplicity, the target field was selected to be the wave field induced by a point source at a point $\vec{r}_o = (5,5)$ located at the center of the square 10×10 2D region. Its spectral distribution is described by (2.13).

Remarks

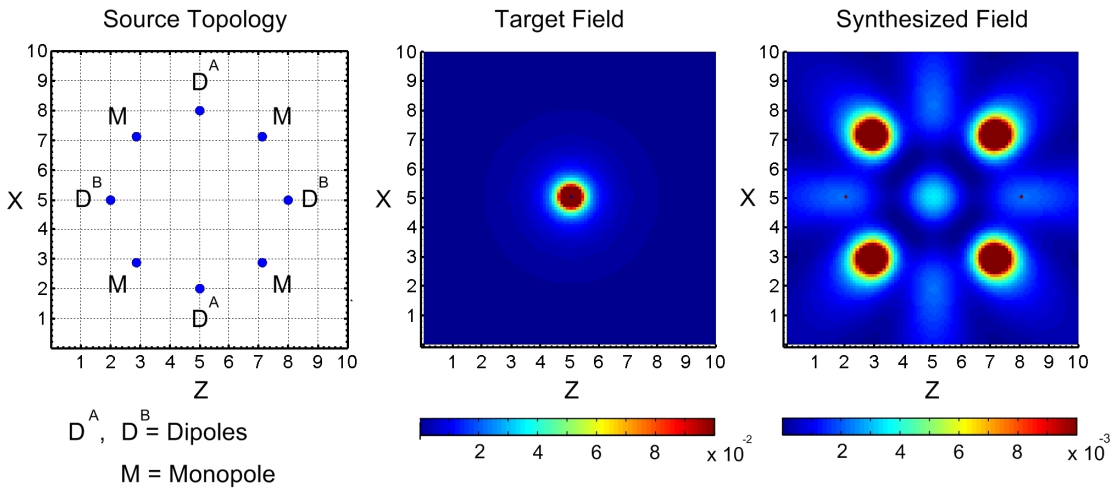

Figure 2.5: Optimal wave field synthesis using sources with different radiation profiles. **Left:** Source Topology. **Center:** Energy distribution of the target field. **Right:** Energy distribution of the synthesized field

Since the synthesis sources are equally distant from the location of the focal point of the target field, one should expect that the power should be equally distributed among the synthesis sources. This does not happen since the proposed process identifies the different radiation profile of the dipole sources and allocates less power to them.

2.4 Conclusions

An optimal spectral acoustic wave field synthesis method was demonstrated for the synthesis of bandlimited wave fields. The method was compared with traditional WFS techniques. Its performance is optimal in the square error sense, overcoming aliasing and truncation problems which appear in its predecessors. Additionally, the method can be applied to arbitrary source topologies, a fact that makes it a potential candidate for sensor network applications. Finally, synthesis sources with different radiation profiles can also be used.

CHAPTER 3

ELECTROMAGNETICS

3.1 Introduction

3.1.1 Antennas and electromagnetic WFS

In antenna theory, wave field synthesis methods appear as solutions to antenna pattern synthesis problems, with applications ranging from single antennas to multi-element topologies like phase arrays and beam-formers. The goal of an antenna pattern synthesis problem is to specify the appropriate current distribution of a single or multiple antenna elements in order to generate a desirable radiation pattern. Early in 1948 Woodward, started investigating this problem [34]. Various techniques were proposed afterwards including: angular prolate spheroidal wave functions by Rhodes [35], Tikhonov regularization in the continuous function domain by Deschamps [36], discrete synthesis methods by Mautz [37] and recently ortho-normal Bessel functions by Chang *et. al*[38].

As antenna structures became more complex, additional elements were added giving more options and flexibilities in synthesizing even more radiation patterns. This led to the introduction of the phase arrays [39],[40] which were developed to replace the mechanically steered radar systems [41]. Since then, phased arrays appeared in many areas including radar systems [42], radio astronomy [43], high frequency on-chip radars [44]-[46] and beam-forming [47]. By allocating appropriate phases to the various elements of a phase array, one can synthesize different radiation patterns and "steer" the main lobe of the antenna at different angles providing different scanning properties. Using the above reasoning we can view an antenna phased array as a wave field synthesis

mechanism [48], which produces wave fields of certain spatial characteristics and steering properties. This synthesis operation has been investigated in the past both in the far and the close field, using spherical vector wave functions [49].

This chapter demonstrates how the wave field synthesis method, analyzed in the previous chapter, can be applied to the synthesis of electromagnetic vector wave fields. The main advantage of this approach is the fact that the proposed method can accommodate arbitrary, not necessary linear, antenna topologies with different radiation characteristics and also provide a precise optimal solution to EM wave field synthesis problems, with guaranteed existence and uniqueness. In this way one can avoid using any iterative, not necessarily convergent optimization schemes in order to solve field synthesis problems. To illustrate this advantage, a theoretical comparison between the performance of a conventional linear phased array and an array using the proposed method, having the same element topology and operating at the same power level, is performed.

3.1.2 Applications

In the medical arena, EM wave field synthesis methods have potential applications in externally controlled drug delivery systems. These systems utilize materials called drug agents to achieve precise delivery of drugs at pathogenic regions of the human body. In this way the treatment becomes more effective. In many cases the drug agents are ferromagnetic materials [50]-[51], which can be moved inside the human body by forces induced by generated magnetic fields. In this way the direction of the movement of the agents is controlled by the induced magnetic fields which must be synthesized accurately. This magnetic field synthesis process can be carried out using the proposed method and utilizing small antenna elements around the human body as distributed wave

sources (Fig. 3.1).

Electromagnetic imaging is another field in which EM wave field synthesis techniques can be applied. When objects with different conductivity or permittivity profiles are illuminated by incident electromagnetic waves, they induce back scattered fields. When these back scattered fields are sampled at a sufficiently dense set of locations, they reveal the shape and the location of their scatterers (initial objects). The above procedure is the basis of electromagnetic imaging which is traditionally treated as an inverse problem [52]. In this problem the input data are the back scattered EM field measurements and the unknowns are the conductivity profiles of the scatterers. Different approaches have been proposed to solve this problem including Genetic Algorithms [53], Conjugate Gradient [54] and Newton-Kantorovich [52] methods. Most of these techniques require post processing of the sensed measurements which is time consuming.

The proposed wave field synthesis technique could be used in order to overcome such difficulties. When EM fields are focused at the points of the objects-scatterers the energy of the back scattered field is maximized. In this way the method can be used to probe the location of objects by synthesizing EM fields focused at different points inside the area of our interest. By measuring the total energy of the back scattered field and collecting the maximum measurements, the locations of the objects-scatterers can be revealed. Furthermore, if the set of focal points is sufficiently dense, the shape characteristics of the scatterers can also be obtained.

The fact that the proposed method can accommodate any multi-source topology can be used in small wireless networks applications [56]. Here we can utilize multi-element antenna arrays [40],[48] in order to generate electromagnetic fields which focus their energy at specific points in space. In this way the communications between the wireless

nodes can be enhanced and multiuser interference can be avoided since the transmitter can focus its field at the receiver's location only.

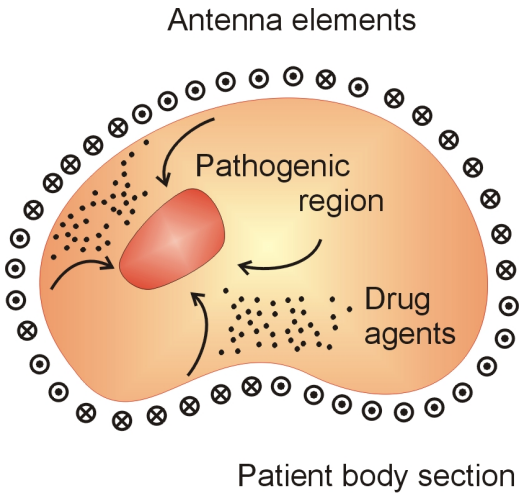

Figure 3.1: Externally controlled drug delivery system

3.1.3 Organization

The rest of the chapter is organized as follows: Section 3.2 contains a theoretical overview. A description of the proposed technique, solutions and generalizations referring to different synthesis experiments are presented in subsection 3.2.1. Subsection 3.2.2 contains the basic properties of the phased arrays. These two subsections serve as the basis for theoretical comparisons which is the topic of section 3.3 of the chapter. The comparisons are based on simulated energy contour plots. These plots are a good criterion for assessment of the quality of the synthesized fields. The chapter concludes with challenges and future directions in 3.4.

3.2 Theory

3.2.1 Generalizations - Solution

Wave field synthesis methods can be extended from the synthesis of scalar acoustic fields to the synthesis of three dimensional electromagnetic vector wave fields. Figure 3.2 illustrates the an EM synthesis process from a system point of view.

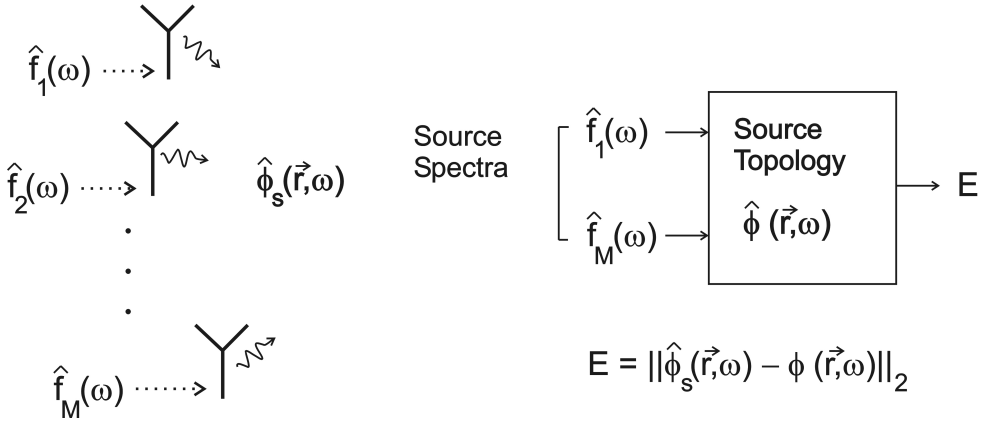

Figure 3.2: EM wave field synthesis (system point of view)

As we did for the case of acoustics we assume that the wave field to be synthesized has a spectral support Ω and that the synthesis region is a set $S \subset R^d$ (d being the number of dimensions). Since EM wave fields are vector fields, generalizations of the solutions referring to the synthesis of scalar wave fields must be applied. If we denote with $\hat{n}_1$,$\hat{n}_2$ and $\hat{n}_3$ the unitary vectors along the three space dimensions, we can solve a three dimensional vector wave field synthesis problem using the solution of a simpler scalar wave field synthesis problem presented in the previous chapter. In three dimensions a vector field spectrum can be expressed as:

$$\hat{\phi}(\vec{r},\omega) = \hat{n}_1\hat{\phi}_1(\vec{r},\omega) + \hat{n}_2\hat{\phi}_2(\vec{r},\omega) + \hat{n}_3\hat{\phi}_3(\vec{r},\omega) \tag{3.1}$$

The scalar wave field synthesis analyzed in the previous chapter can be applied here individually for each dimension. Initially, one has to define the error function as the sum of the error norms in all dimensions. If k is the index of each dimension then the error norm can be defined as:

$$\begin{aligned} E &= \sum_{k=1}^{3} \left\| \hat{\phi}_k(\vec{r},\omega) - \hat{\phi}_{ks}(\vec{r},\omega) \right\|_2^2 \\ E &= \sum_{k=1}^{3} \int_S \left[\int_{-\infty}^{\infty} \left| \hat{\phi}_k(\vec{r},\omega) - \hat{\phi}_{ks}(\vec{r},\omega) \right|^2 d\omega \right] d\vec{r} \end{aligned} \tag{3.2}$$

If we assume that the total number of distributed sources performing the synthesis is M then the synthesized scalar field of the k^{th} dimension will be:

$$\hat{\phi}_{ks}(\vec{r},\omega) = \sum_{j=1}^{M} \begin{cases} \hat{f}_j(\omega) G_{kj}(\vec{r},\omega) & \omega > 0 \\ 0 & \omega = 0 \\ \hat{f}_j^*(-\omega) G_{kj}^*(\vec{r},\omega) & \omega < 0 \end{cases} \tag{3.3}$$

In the case of multi-element antenna configurations the function $\hat{f}_j(\omega)$ refers to the spectrum of the current of the j^{th} element $\hat{I}_j(\omega)$ and $G_j(\vec{r},\omega)$ to its radiation pattern $D_j(\vec{r},\omega)$. As it was done for the scalar acoustic fields equation (3.2) express the synthesis error measure E as a function of the source spectra $\{\hat{f}_j(\omega)\}$. As it was analyzed in the previous chapter the goal of the proposed method, is to find the optimal source spectra which minimize this measure:

$$\{\hat{f}_j^{opt}(\omega)\} = \min_{\{\hat{f}_j(\omega)\}} \left[E(\{\hat{f}_j(\omega)\}) \right] \tag{3.4}$$

It is easy to show that in this case the Σ_o solution determined by equation (2.8) has to be modified to:

$$\{\hat{x}_0\} = \arg \min_{\hat{f}_j(\omega) \in \Sigma_0} \left[E(\{\hat{f}(\omega)\}) \right] \tag{3.5}$$

where

$$\begin{aligned}
&\{\hat{x}_0\} = \{\hat{x}_{01}, ..., \hat{x}_{0M}\} \\
&\{\hat{x}_0\} = [H]^{-1}\{l\} \\
&[H] \in C^{M \times M}, \quad \{l\} \in C^{M \times 1} \\
&[H]_{pq} = \sum_{k=1}^{3} \int_S \left[\int_\Omega G_{kp}(\vec{r}, \omega) G_{kq}^*(\vec{r}, \omega) d\omega \right] ds \\
&\{l\}_q = \sum_{k=1}^{3} \int_S \left[\int_\Omega \hat{\phi}_k(\vec{r}, \omega) G_{kq}^*(\vec{r}, \omega) d\omega \right] ds \\
&p, q \in \{1, ..., M\}
\end{aligned} \tag{3.6}$$

3.2.2 Phased arrays

A typical linear phased array is characterized by the steering angle θ. This angle is implemented by a phase difference of

$$\delta\phi = \frac{2\pi}{\lambda}(d \sin\theta) \tag{3.7}$$

radians between neighbor sources [40].

3.3 Comparison

The goal of this section is to compare the energy distribution of the wave field induced by the proposed EM wave synthesis technique with the energy distribution of the field of a linear phased array, operating at the same total power level and having the same element topology. This comparison was implemented by three separate experiments. In each of the experiments the target field was the field induced by a point source at $\vec{r}_o$ (focal point) with unity flat spectrum in the band $\Omega = [2\pi(f_c - f_s), 2\pi(f_c + f_s)]$ $\forall\omega \in \Omega \;\; \hat{f}(\omega) = 1$. In other words the spectrum distribution of the k^{th} component of the target vector field is:

$$\hat{\phi}_k(\vec{r}, \omega) = G_o(\vec{r}, \omega) = \frac{e^{-i\frac{\omega}{c}|\vec{r}-\vec{r}_o|}}{4\pi|\vec{r} - \vec{r}_o|} \;\; \forall\omega \in \Omega \tag{3.8}$$

The region S used in every synthesis experiment according to (3.6) was a square centered at the focal point point $\vec{r}_o = (X_o, Y_o)$ with side 100 space units ($\{(x, y), \;\; |x - X_o| <= 100, |y - Y_o| <= 100\}$).

3.3.1 Energy distribution and figure of merit

In order to assess the quality of the synthesized field we plotted the contour plot of the energy distribution which is given at each point $\vec{r}$ by the following integral:

$$E(\vec{r}) = \frac{1}{2\pi}\int_{\Omega} |\hat{\phi}(\vec{r}, \omega)|^2 d\omega \tag{3.9}$$

The comparison between the performance of proposed EM wave synthesis method applied to a certain element topology and the performance of a phased array applied to the same topology has to be done in the same total delivered energy levels. The total delivered energy is proportional to the actual total delivered energy to the elements. The last can be calculated generally by:

$$E_{del} = \frac{1}{2\pi} \int_{\Omega} \{\hat{f}(\omega)\}^H \{\hat{f}(\omega)\} d\omega \tag{3.10}$$

For the Σ_o solution ($\{\hat{x}_0\}$ in (3.6)) the above expression is simplified to:

$$E_{del} = \frac{1}{2\pi} \{\hat{x}_0\}^H \{\hat{x}_0\} (4\pi f_s) \tag{3.11}$$

with $\mu(\Omega) = (4\pi f_s)$ being the total length of the frequency band $\Omega = [2\pi(f_c - f_s), 2\pi(f_c + f_s)]$. Based on the calculation of the delivered energy we can define the figure of merit at a point $\vec{r}$ as the ratio of the energy of the synthesized field at this point (calculated based on equation (3.9)) to the total delivered energy:

$$f_m(\vec{r}) = \frac{E(\vec{r})}{E_{del}} \tag{3.12}$$

Generally, the greater the figure of merit the higher field energy concentration is achieved.

3.3.2 Different element topologies

In the first synthesis experiment the proposed EM wave synthesis method was compared with a regular linear phased array technique. Ten equally distant omnidirectional

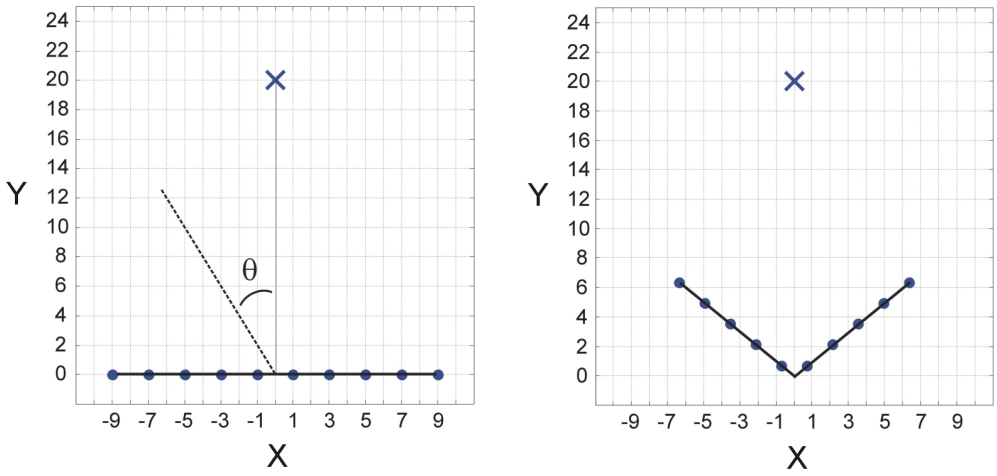

Figure 3.3: **Left:** Linear array of wave sources, **Right:** V-shape array of wave sources

monopole sources $d = 15mm = \frac{\lambda}{2}$ apart were considered ($\lambda = 30mm$, $f_c = 10GHz$). Fig. 3.3 displays the set up using a space scale in which 1 space unit $= 7.5mm$ and $\lambda = 4$space units. Using the proposed technique, we designed the signals of the ten wave sources in order to synthesize the wave field induced by a point wave source at $\vec{r}_o = (X_o, Y_o) = (0, 5\lambda) = (0, 20\text{space units}) = (0, 150mm)$ (indicated with "x" in Fig. 3.3) with unity flat spectrum in $\Omega = [2\pi(f_c - f_s), 2\pi(f_c + f_s)]$ ($f_s = 10MHz$ and $f_c = 1GHz$). The resulting figure of merit distribution according to (3.12) is displayed in the center plot of Fig. 3.4.

In order to compare our technique with a phased array operating in the same energy level, we considered a 10 element phased array in which the delivered energy in each element equals $\frac{E_{del}}{10}$ (with E_{del} the total delivered energy according to (3.11)). In order to achieve best performance at the point $\vec{r}_o = (X_o, Y_o) = (0, 5\lambda)$, the steering angle of the phased array was chosen to be zero radians (all the sources are in phased according to (3.7)). The resulting figure of merit distribution of this phased array is displayed in the left plot of Fig. 3.4.

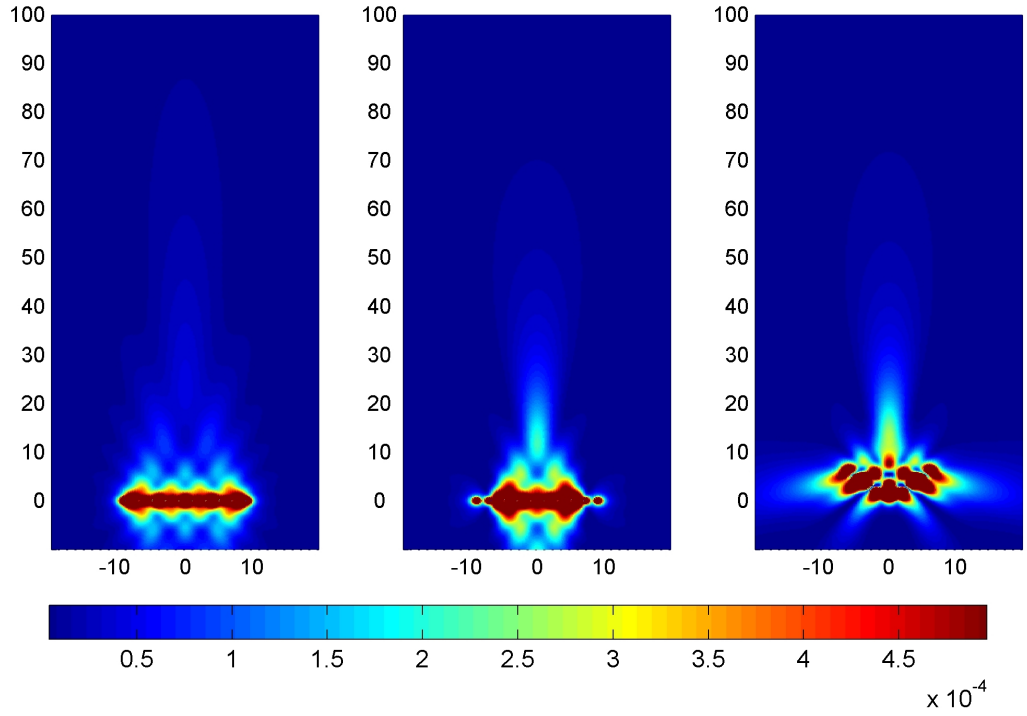

Figure 3.4: **Left**: Figure of merit of the synthesized field using a linear phased array, **Center**: Figure of merit of the synthesized field using the proposed technique on a linear array, **Right**: Figure of merit of the synthesized field using the proposed technique on a v-shape array

Finally, we considered a v-shape arrangement of the 10 sources according to the right plot of Fig. 3.3. As we did in the linear case we implemented the proposed synthesis technique for the same wave field (Source point: $\vec{r}_o = (X_o, Y_o) = (0, 5\lambda) = (0, 20)$, $f_s = 10MHz$ and $f_c = 10GHz$). The resulting figure of merit distribution is displayed in right plot of Fig. 3.4.

The ratio of figure of merit of the linear array to the figure of merit of the regular phased array at the point $(X, Y) = (0, 5\lambda)$ was 2.3629. The same ratio referring to the figure of merits of the v-shape array and the regular phased array at the same point was 2.4608. Clearly the v-shape arrangement achieves higher field concentration at the point $\vec{r}_o$.

Discussion: Comparing the contour plots of Fig. 3.4, we observe that our method achieves higher energy values concentrated around the point $\vec{r}_o = (X_o, Y_o) = (0, 5\lambda)$, compared with a regular phased array. The concentration is increased as the geometry changes from linear to a v-shape arrangement. This property could be used in medical applications where the goal is to achieve high intensity field values at specific points using non linear element topologies (elements distributed around the human body). Consequently, using the proposed technique, we could achieve best focusing given any array geometry.

3.3.3 Different Focal Points

The characteristics of the synthesized field using the proposed wave field synthesis method depend on the location of the point of the synthesis. In order to illustrate this, we compared the performance of a regular linear phased array with the performance of a linear array using the proposed technique and focusing the wave energy at different points in space. The linear arrangement of the first experiment was repeated here (left plot of Fig. 3.3). The location of the focal point was varied. Starting from the origin $(0, 0)$ and following a constant angle $\theta = 0^o$ we increased the distance R from the origin with increments equal to the wavelength $\lambda = 4$ space units ($R = k\lambda$, $k = 0, ..., 20$). This way 21 focal points including the origin, are defined. The ratio of the figure of merit achieved by the regular phased array to the figure of merit achieved by the same linear array using the proposed technique was calculated at the previous points. The same process was repeated for angles $\theta = 45^o$ and $\theta = 90^o$ by "steering" the regular phased array at angle θ and by synthesizing a point field at $\vec{r}_o = (X_o, Y_o) = (R\cos\theta, R\sin\theta)$, using the proposed method. The respective ratios of figures of merit referring to these three steering angles as functions of the distance from the origin, are displayed in Fig. 3.5.

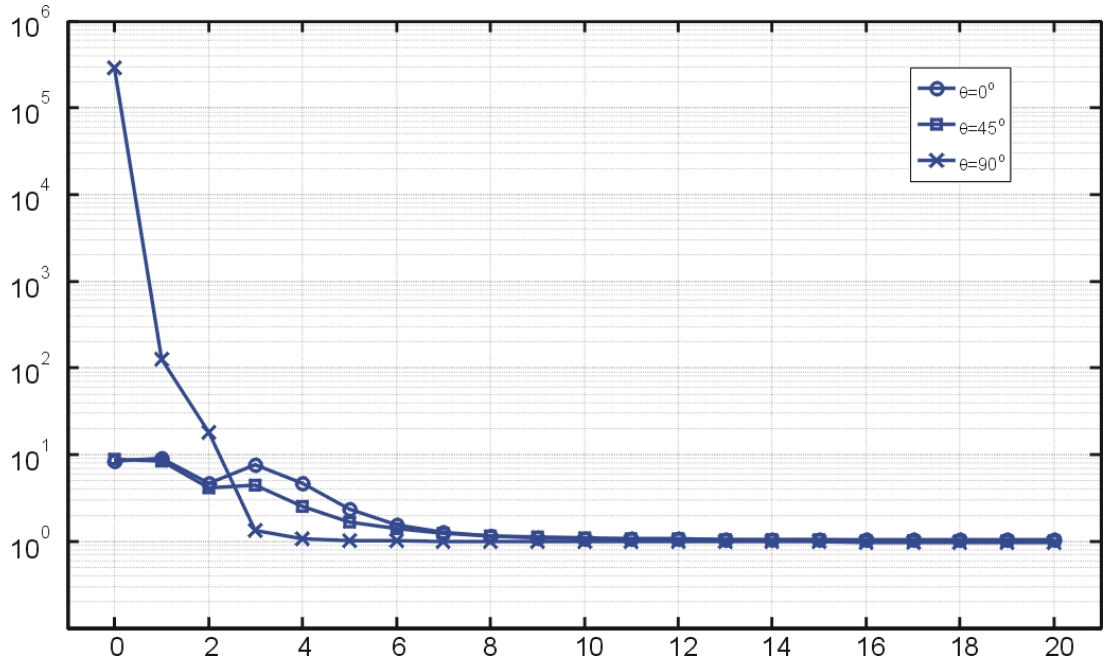

Figure 3.5: Ratio of figure of merit of WFS over the figure of merit of the linear phased array technique, as a function of the distance of the focal point from the origin in wavelengths for different steering angles

Discussion: Looking at Fig. 3.5, it is obvious that the near field energy concentration achieved by the proposed method compared with the one achieved by the regular phased array is higher. Especially for $\theta = 90^o$ this difference is relatively big for the focal points near the origin. As the focal point moves far from the origin the energy concentrations converge asymptotically to the same level.

3.3.4 Different number of elements

In order to study the energy concentration as a function of the number of distributed wave sources and compare the quality of the synthesis achieved by the proposed method with the one achieved by a regular phased array, the following experiment was performed. The linear array displayed at the left plot of Fig. 3.3 was considered again.

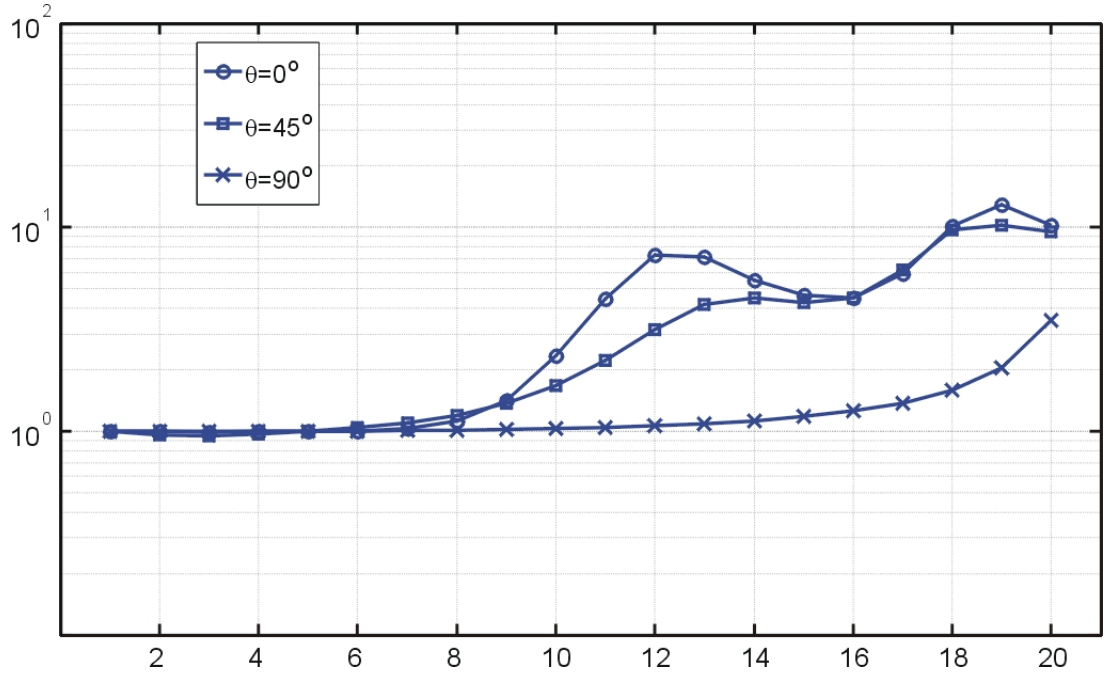

Figure 3.6: Ratio of figure of merit of WFS over the figure of merit of the linear phased array technique, as a function of the total number of elements used for synthesis for different orientation angles

This time the distance of the focal point from the origin was kept constant equal to $R = 5\lambda$. Different number of sources were used each time ranging from 2 to 20 forming a linear array with the same origin $(0, 0)$ and equally distant sources ($d = \frac{\lambda}{2}$) each time. The ratios of the figure of merit of the proposed technique to the figure of merit of the linear phased array were calculated as a function of the number of sources. Three graphs referring to angles $\theta = 0^o$, $\theta = 45^o$ and $\theta = 90^o$ were obtained. The coordinates of the focal points were given by $(X, Y) = (R\cos\theta, R\sin\theta) = (5\lambda\cos\theta, 5\lambda\sin\theta)$. The obtained figure of merit ratio graphs referring to the three steering angles are displayed in the plot of Fig. 3.6.

Discussion: Fig. 3.6 suggests that as long as the number of sources are greater than 9 the proposed method achieves higher energy concentration at the focal point than concentration achieved by the regular phased array. As the number of elements

decreases the energy concentrations converge to the same level as it is expected.

3.3.5 Directional elements

In order to illustrate the applicability of the proposed method on directional wave sources we considered a magnetic field synthesis experiment using antenna Hertz dipoles. As antenna theory suggests, the radiation pattern of a hertz dipole exhibits certain directional characteristics that can be utilized by the proposed technique. More precisely the spectrum of the magnetic vector field induced by a dipole of length L, at $\vec{r}_j$ contains only the azimuth ($\hat{\phi}$) component and is given by:

$$\begin{aligned} \vec{H}(\vec{r},\omega) &= \hat{I}_j(\omega) D_{j\phi}(\vec{r},\omega)\hat{\phi} \\ D_{j\phi}(\vec{r},\omega) &= \left[\frac{L}{4\pi|\vec{r}-\vec{r}_j|} e^{-ik|\vec{r}-\vec{r}_j|}\left(ik+\frac{1}{|\vec{r}-\vec{r}_j|}\right)\sin(\theta)\right] \end{aligned} \tag{3.13}$$

The parameter one has to specify in order to perform magnetic field synthesis with Hertz dipoles is the spectrum of their current $\hat{I}_j(\omega)$. In order to use proposed wave field synthesis method, the spectral functions $G_j(\vec{r},\omega)$ in equations (2.8), (3.6) and (2.9) must be replaced by the functions $D_{j\phi}(\vec{r},\omega)$, $j = 1, ..., M$ of (3.13). The rest of the calculations remain the same.

The linear topology of the left plot of Fig. 3.3 was considered again for the synthesis experiment in this case. Directional dipoles were used instead of omnidirectional elements. The bandwidth parameters of Ω were $f_c = 75GHz$ and $f_s = 1MHz$. Initially a wave field induced by a point source at $\vec{r}_o = (X_o, Y_o) = (0, 20)$ was optimally synthesized using the proposed technique on an array of 10 directional dipoles placed at a line along the x axis with origin the point $(0, 0)$ (refer to the left plot of Fig. 3.3). This field was

compared with a field induced by a 10 element phased array using the same directional dipoles, at the same locations and with same total input power. The steering angle of the array was set at $\theta = 0^o$. For simplicity we considered the length of each element to be $L = 1$ (3.13).

Fig. 3.7 displays the energy distribution of the synthesized field in both cases. The third plot also provides the distribution of the logarithm of the ratio of the energies at each point:

$$R = \log\left[\frac{E^{dir}}{E^{omndir}}\right] \tag{3.14}$$

Discussion: It is justified from the contour plots of Fig. 3.7 that field values achieved at the focusing point (0,20) using the proposed field synthesis method on directional dipoles are higher than the field values induced using a regular phased array method on the same dipoles and consuming the same total energy. Magnetic field focusing using the proposed field synthesis techniques could have potential medical applications in externally controlled drug delivery systems.

3.4 Conclusions and future directions

The extension of the proposed wave field synthesis method from the synthesis of acoustic scalar wave fields to the synthesis of generally described electromagnetic vector wave fields was the main of this chapter . The method appears to have potential future applications on antenna arrays for imaging purposes, in wireless LANs and medicine. Any application which involves large arrays of distributed antennas with not necessarily linear topology can also benefit from this method. Compared with phased arrays, the

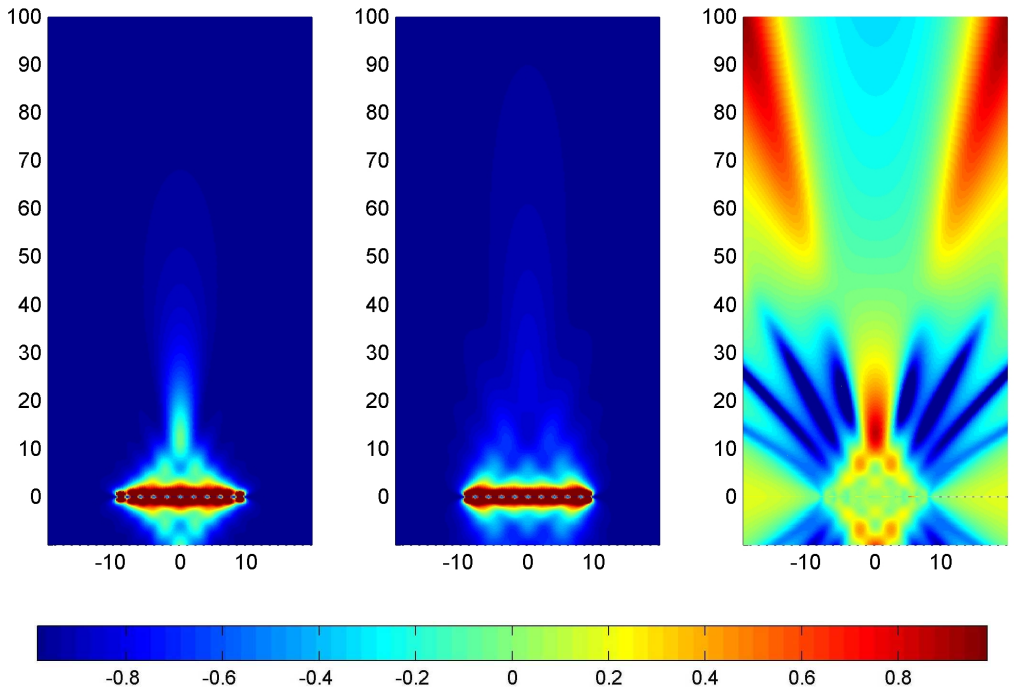

Figure 3.7: **Left:** Energy distribution of synthesized field using the proposed technique, focused at the point (0,20), with directional dipoles, **Center:** Energy distribution of synthesized field of a phased array (with $\theta = 0^o$) using directional dipoles, **Right:** Plot of the logarithm of the ratio of the energy distribution of the synthesized field using the proposed technique on directional dipoles (left plot) over the energy distribution of the synthesized field of a phased array of directional dipoles (center plot), **Colorbar:** Refers to the logarithmic plot.

proposed technique gives better results in terms of energy concentration in the near field and asymptotically the same results in the far field.

Perhaps one of the biggest obstacles towards a successful wave field synthesis experiment is the fact the the underlying wave medium could be inhomogeneous anisotropic and non-linear. Moving charged particles could potentially alter the electromagnetic properties of the medium and therefore introduce inhomogeneities. In such scenarios knowledge of the inhomogeneity is required. The error minimization concept of proposed wave field synthesis method can be used in this case with the aid of numerical schemes obtained by finite element [18] discretization methods [19]. Given a fixed dis-

cretization scheme, the computation time of these techniques increases exponentially with the size of the synthesis region. Therefore, ways of carrying out these computations faster could be investigated.

CHAPTER 4

WAVE FIELD SYNTHESIS IN NONLINEAR LC LATTICES

4.1 Introduction

4.1.1 LC lattices and nonlinear WFS

Wave synthesis phenomena can be created not only inside continuous acoustic or electromagnetic media but also in periodic structures [57]. An example of such structure is the two dimensional nonlinear LC lattice in which electromagnetic wave fields with certain spatial characteristics can be synthesized.

A two dimensional nonlinear LC lattice is an electrical circuit consisting of identical, repeated in two dimensions, small LC elements. Each LC element consists of two coils and a non-linear capacitor or varactor connected as illustrated in Fig. 4.1. The inputs of the lattice are voltage sources applied at the left and bottom side as Fig. 4.1 displays. The behavior of a LC-lattice emulates the behavior of a two dimensional wave medium. Therefore wave synthesis principles can be applied here. Furthermore, under certain conditions such lattices exhibit rich non-linear behavior. This behavior is the topic of the present chapter.

If the capacitors of the lattice are constant with respect to their applied voltage the lattice has similar properties to a continuous linear wave medium [57]. Furthermore, if the voltage sources are in phase the electromagnetic waves originating from them propagate and add up along the main diagonal of the lattice, inducing amplified waveforms in the center of the lattice. The linear nature of the lattice ensures that the frequencies of the signals observed in the intermediate nodes appear also in the inputs.

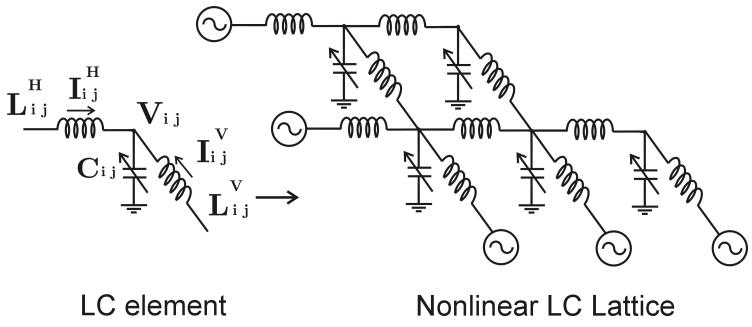

Figure 4.1: Nonlinear two dimensional LC lattice

However if the capacitance value changes with respect to their applied voltage, the lattice emulates a non-linear wave medium which is characterized by a wave-speed which depends on the wave amplitude. In this case, due to the non-linearity the amplification observed in the center of the lattice can be considerably higher than that of the linear case. Additionally, higher frequency components than the input frequencies appear in the central nodes. By biasing the capacitors using an external DC voltage source at a certain optimal operating voltage range, the input pulses generated by the voltage sources in the boundaries can be added in the central nodes and significantly amplified and sharpened. This nonlinear constructive wave synthesis phenomenon can be explained by the high amplitude and high frequency harmonic generation observed in such lattices and is illustrated in the figure 4.2.

The high amplitude and high frequency harmonic generation which characterizes the behavior of a nonlinear two dimensional LC lattice can be studied theoretically using the method of perturbations. In order to do that an approach similar to a Finite Element procedure [18] must be followed. Initially, every LC unit is treated as a finite element with governing equations, the voltage and current Kirchhoff laws. These equations are assembled into a unique system equation referring to the whole lattice.

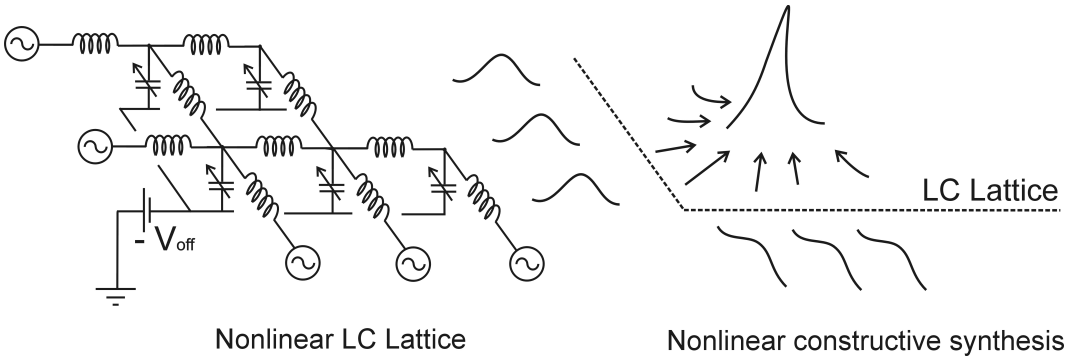

Figure 4.2: Amplification and sharpening of input pulses in the center nodes of a two dimensional nonlinear LC lattice

4.1.2 Potential applications

The high frequency and high amplitude harmonic generation ability of the examined nonlinear LC lattice, holds a promise of creating electronic devices which will fill in the Tera-Hertz gap (Fig. 4.3 [58]). This gab has been formed by the present device technology, which is not mature enough to provide a big number of devices operating at relatively high power levels at the Tera-hertz frequency range (100 GHz to 10 THz).

Radiation in the Tera-Hertz range can provide high resolution with minimum health risks, since it is not ionizing. Therefore nonlinear devices such as nonlinear two dimensional LC lattices, could be embedded in existing devices and expand further their frequency and power performance, materializing the advantages the Tera-hertz technology can offer. Such devices could be oscillators or frequency multipliers for high data rate communication and imaging systems, which can be used for security and medical purposes.

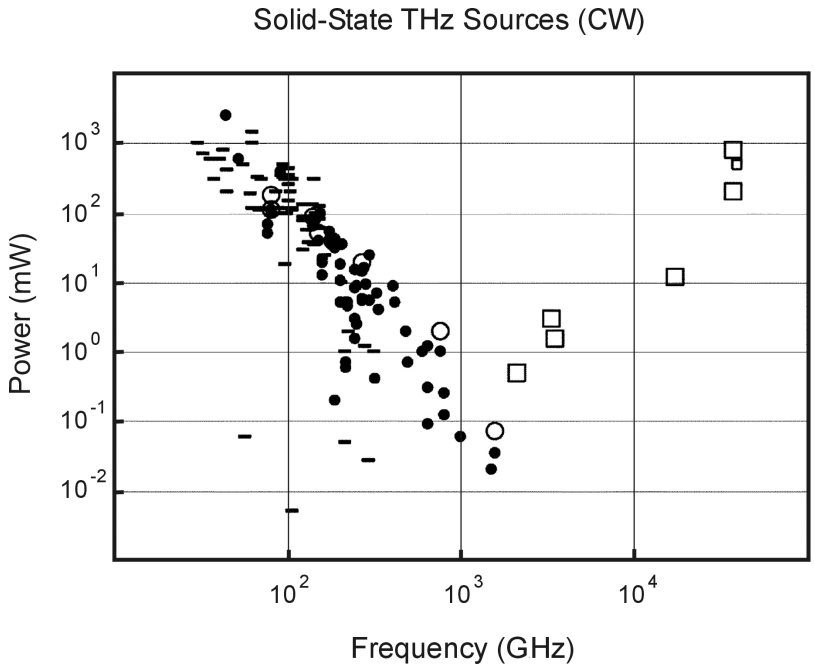

Figure 4.3: Terahertz gap with respect to source technology. Quantum cascade lasers (□) are progressing downward from higher frequencies, while electronic technology is progressing upward. Frequency multipliers (•) dominate other electronic devices (-) above about 150 GHz. Cryogenic results are shown as hallow symbols.

4.1.3 Prior Art

The solutions of the governing equations of two dimensional nonlinear lattices were studied by many authors. Traveling wave solutions of the governing equations of nonlinear 2D Sine Gordon dynamical lattices [59, 60, 61], also known as Frenkel-Kontorova (FK) models, were investigated in [62]. The existence of time periodic, space localized solutions (called discrete breathers), is investigated generally in [63] and for the case of sine-Gordon lattices in [64]. Discrete breathers can be found also in Fermi Pasta Ulam (FPU) lattices, which are associated with nonlinear LC lattices. This has been demonstrated for the case of rectangular [65] and hexagonal [66] LC lattices. The excitation of internal modes appears in nonlinear lattices as it is illustrated in [67]. The generation

of pattern formations in Klein Gordon lattices is analyzed in [68]. Finally the equations governing the behavior of a two dimensional nonlinear LC lattice are derived and solved using the method of perturbations, for specific types of nonlinearities in [69].

Experimental work on one and two dimensional nonlinear LC-lattices has also been performed. The idea of producing electrical solitons using nonlinear transmission lines (a 1-D version of the lattice) has been studied extensively for nearly 50 years [70, 71, 72], and has been demonstrated on chips with GaAs [73, 74] and Si [75, 76, 77] substrates. In 1980, Ostroviskii *et al.* [78] studied soliton formation caused by resonance phenomena in two dimensional nonlinear LC lattices with perfectly reflecting boundaries. Stepanyants measured the Cerenkov radiation caused by wave propagation in two dimensional nonlinear LC lattices in 1984 [79], a phenomenon which also appears in the sea wave patterns generated at the back of traveling ships.

4.1.4 Organization

The theoretical basis for the development of the system of nonlinear partial differential equations governing the behavior of a LC lattice is presented initially in section 4.2. Two solutions of this system of equations are proposed: one analytical based on the method of perturbations referring to certain types of nonlinearities (subsection 4.2.1) and a more general numerical solution (section 4.2.2). Spectrum analysis is also performed in order for the frequency eigen-modes to be specified.

Simulation results using the developed numerical approach are discussed in section 4.3 of the chapter. A two dimensional frequency plot, containing the lattice responses when it is excited by various input frequencies, is also presented in subsection 4.3.2. This plot reveals the nonlinear frequency shifting properties of the lattice.

The theoretically derived properties studied in sections 4.2 and 4.3 are verified experimentally with a series of experiments in section 4.4. The goal of these experiments was to determine the optimal conditions under which maximum amplification and frequency shift are observed at the middle nodes of the lattice.

4.2 Theory

4.2.1 Finite element approach using the method of perturbations

In order to study the nonlinear wave interactions in a general $N \times N$ LC lattice we have to express the coupled governing current/voltage equations at the LC element level. These are the Kirkhoff voltage and current laws. These laws referring to the i, j ($(i, j) \in \{1, ..., N\} \times \{1, ..., N\}$ Fig. 4.4) node of the lattice are:

$$\begin{aligned} \frac{\partial}{\partial t} \int_{V_{i,j}} C_{i,j}(V_{i,j}) dV_{i,j} &= I^H_{i,j} + I^V_{i,j} - I^H_{i,j+1} - I^H_{i+1,j} \\ L^H_{i,j} \frac{\partial I^H_{i,j}}{\partial t} &= V_{i,j} - V_{i,j-1} - r I^H_{i,j} \\ L^V_{i,j} \frac{\partial I^V_{i,j}}{\partial t} &= V_{i,j} - V_{i-1,j} - r I^V_{i,j} \end{aligned} \tag{4.1}$$

where $C_{i,j}, L^H_{i,j}, L^V_{i,j}$ are the capacitance and the inductances of the vertical and horizontal edge of the LC element with node i, j. The fact that the inductors are non ideal is modeled by a small ohmic resistance r. The node voltage and the flowing currents in the horizontal and vertical edge of the LC element i, j are denoted by $V_{i,j}, I^H_{i,j}$ and $I^V_{i,j}$.

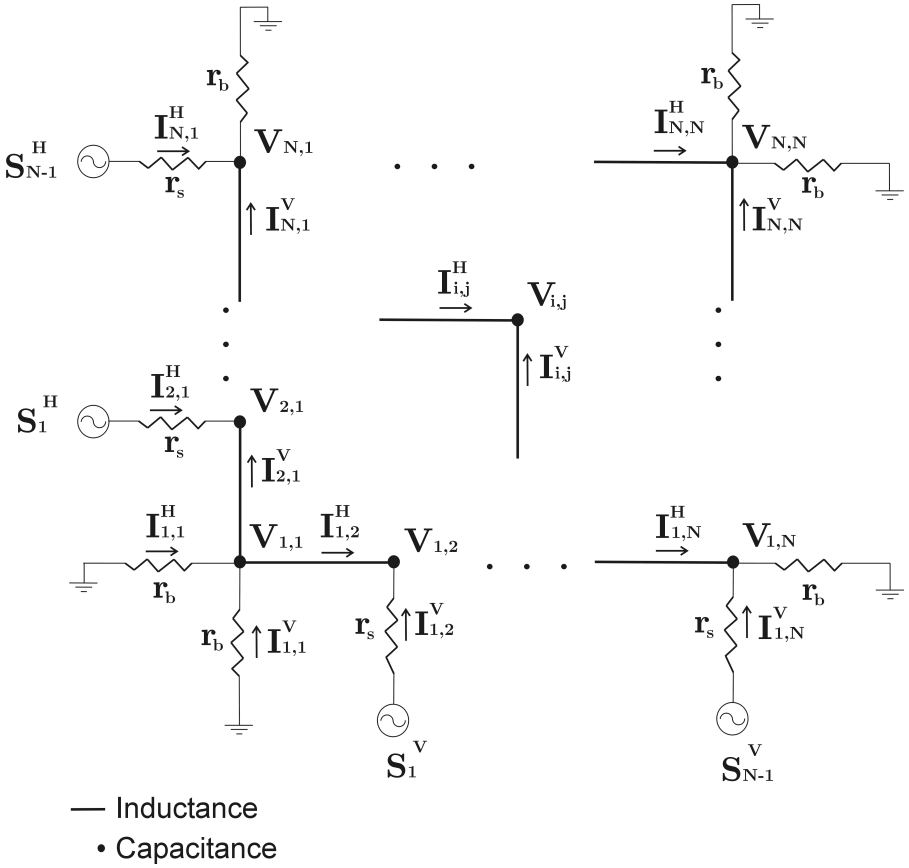

Figure 4.4: Modeling of two dimensional LC lattice

For small perturbations around a fixed voltage value a linear relation between the capacitance and the observed voltage value at the node i, j can be assumed, i.e:

$$C_{i,j}(V_{i,j}) = C_o(1 - bV_{i,j}) \tag{4.2}$$

Applying (4.2) to the element equations (4.1) leads to:

$$\begin{aligned} C_o\frac{\partial V_{i,j}}{\partial t} &= I^H_{i,j} + I^V_{i,j} - I^H_{i,j+1} - I^H_{i+1,j} + bC_oV_{i,j}\frac{\partial V_{i,j}}{\partial t} \\ L^H_{i,j}\frac{\partial I^H_{i,j}}{\partial t} &= V_{i,j} - V_{i,j-1} - rI^H_{i,j} \end{aligned}$$

$$L^V_{i,j}\frac{\partial I^V_{i,j}}{\partial t} = V_{i,j} - V_{i-1,j} - rI^V_{i,j} \tag{4.3}$$

As one can observe, the nonlinearity is introduced by the last term of the first equation of (4.3).

Our next step towards establishing a global system of equations describing the behavior of the whole lattice is to define a mapping from the "local" node coordinates (i, j) to a "global" system index k. This mapping can be obtained using the following expression:

$$\begin{aligned} &k = i + (j-1)N \\ &(i, j) \in \{1, ..., N\} \times \{1, ..., N\} \\ &k \in \{1, ..., N^2\} \end{aligned} \tag{4.4}$$

Then based on the above mapping we define a state vector $\{w\} = \{V_{1:N^2}, I^H_{1:N^2}, I^V_{1:N^2}\}$ as follows:

$$\{w\} = \{V_{1,1}, ..., V_{N,N}, I^H_{1,1}, ..., I^H_{N,N}, I^V_{1,1}, ..., I^V_{N,N}\} \tag{4.5}$$

In order to express a global system equation combining all of the equations (4.3) we have to define a source voltage vector $\{s\}$:

$$\{s\} = \{0_{N^2}, s^H_{1:N^2}, s^V_{1:N^2}\}$$

$$\{s^H_{1:N^2}\} = \{0, S^H_{1:N-1}, 0_{N(N-1)}\}$$
$$\{s^V_{1:N^2}\} = \{0_N, S^V_1, 0_{N-1}, S^V_2, 0_{N-1}, ..., 0_{N-1}, S^V_{N-1}\} \tag{4.6}$$

and boundary currents:

$$\begin{aligned}
I^H_{1,1} &= \frac{V_{1,1}}{r_b} \\
I^V_{1,1} &= \frac{V_{1,1}}{r_b} \\
I^H_{i+1,1} &= \frac{1}{r_s}(S^H_i - V_{i+1,1}) \quad i = \{1, ..., N-1\} \\
I^V_{1,j+1} &= \frac{1}{r_s}(S^V_j - V_{1,j+1}) \quad j = \{1, ..., N-1\} \\
I^H_{i,N+1} &= \frac{V_{i,N}}{r_b} \quad i = \{1, ..., N\} \\
I^V_{N+1,i} &= \frac{V_{N,i}}{r_b} \quad j = \{1, ..., N\},
\end{aligned} \tag{4.7}$$

where r_b is the boundary termination resistance of the lattice and r_s is the source resistance.

In practice $r_s \approx 0$ and therefore we can assume that:

$$\begin{aligned}
V_{i+1,1} &\approx S^H_i \quad i = \{1, ..., N-1\} \\
V_{1,j+1} &\approx S^V_j \quad j = \{1, ..., N-1\}
\end{aligned} \tag{4.8}$$

The previous currents and voltages (contained in the voltage and source vectors $\{w\}$ and $\{s\}$) are displayed analytically in Fig. 4.4.

The boundary vector $\{s\}$ describes the external driving voltage sources. Given the boundary conditions of (4.6),S equations (4.3) can be assembled in a global system:

$$[E]\{\frac{\partial w}{\partial t}\} = [F]\{w\} + \{s\} + b[C]\{w\}.\{\frac{\partial w}{\partial t}\}, \tag{4.9}$$

where [E] is a diagonal matrix containing the capacitance C_o and inductance values $L^H_{i,j}$, $L^V_{i,j}$ and [F] is a sparse matrix containing 1.-1 and r values depending on the lattice node connections. The matrix $[C]$ is the following capacitance matrix:

$$[C] = \begin{bmatrix} C_o I_{N\times N} & 0_{N\times N} & 0_{N\times N} \\ 0_{N\times N} & 0_{N\times N} & 0_{N\times N} \\ 0_{N\times N} & 0_{N\times N} & 0_{N\times N} \end{bmatrix} \tag{4.10}$$

In order to solve for the vector $\{w\}$ using the method of perturbations, we have to express $\{w\}$ as a power series of the nonlinear coefficient b:

$$\{w\} = \{w_0\} + b\{w_1\} + b^2\{w_2\} + ... \tag{4.11}$$

plugging (4.11) into (4.9) and isolating the coefficients of the powers of b, leads to:

$$[A_0(w_0)] + b[A_1(w_0, w_1)] + b^2[A_2(w_0, w_1, w_2)] + ... = 0 \tag{4.12}$$

Where A_k is an expression of the vectors $\{w_0\}, ..., \{w_k\}$.

$$A_0(w_0) = [E]\{\frac{\partial w_0}{\partial t}\} - [F]\{w_0\} - \{s\}$$

$$A_n(w_0, ..., w_n) = [E]\{\frac{\partial w_n}{\partial t}\} - [F]\{w_n\} - [C] \sum_{l+m=n-1} \{w_l\}.\{\frac{\partial w_m}{\partial t}\} \tag{4.13}$$

In order (4.12) to be true for every value of b all the expressions A_n must be equal to zero, i.e.:

$$\begin{aligned} [E]\{\frac{\partial w_0}{\partial t}\} &= [F]\{w_0\} - \{s\} \\ [E]\{\frac{\partial w_n}{\partial t}\} &= [F]\{w_n\} - [C] \sum_{l+m=n-1} \{w_l\}.\{\frac{\partial w_m}{\partial t}\} \end{aligned} \tag{4.14}$$

Taking the fourier transform of the last set of equations leads to the following systems:

$$\begin{aligned} \{\hat{w}_0\} &= \left[j\omega[E] - [F]\right]^{-1} \{\hat{s}\} \\ \{\hat{w}_n\} &= \left[j\omega[E] - [F]\right]^{-1} [C] \sum_{l+m=n-1} \{\hat{w}_l\} * \{j\omega\hat{w}_m\} \end{aligned} \tag{4.15}$$

Here, the element by element multiplication in the time domain is replaced by convolution in the frequency domain.

Remarks

Equations (4.15) suggest an iterative way of determining the components $\{\hat{w}_i\}$ of the expansion of the system solution. As one can observe, the key point here is the inversion of the matrix:

$$[M(\omega)] = \left[j\omega[E] - [F] \right] \tag{4.16}$$

There is a specific frequency $\omega_{cutoff} = 2\pi f_{cutoff}$ after which the magnitudes of all of the eigenvalues of the matrix $[M(\omega)]$ are increasing considerably, forcing the output of the lattice (voltages and currents) to be subsided. This cutoff frequency can be identified by plotting the magnitude of the minimum eigenvalue of the matrix $[M(\omega)]$ versus the frequency ω. It can be shown [69], that for a linear lattice with constant capacitance C, coils with inductance L and resistance r, the cutoff frequency can be derived by:

$$f_{cutoff} = \frac{\sqrt{8}}{2\pi\sqrt{LC}} \tag{4.17}$$

Furthermore, it is apparent that $\{\hat{w}_0\}$ represents the linear part of the solution and $\{\hat{w}_i\}, (i > 0)$ represents the non-linear terms since the convolution $\{\hat{w}_l\} * \{j\omega\hat{w}_m\}$ amplify higher order frequency harmonics of the previous solutions. However this higher harmonics amplification is considerably reduced due to the cutoff frequency bound. If we assume that the input of the lattice is a pure tone at frequency ω_o then the result of the convolution introduced by the nonlinear terms (b terms) of equation (4.15) will be the generations of multiple tones at frequencies $\omega = n\omega_o, \quad n \in N$.

Therefore, there exist an integer $n_{cutoff} = \lfloor \frac{\omega_{cuttoff}}{\omega_o} \rfloor$ such that for $n > n_{cutoff}$ inversion of $[M(n\omega_o)]$ will be subsided considerably. Consequently terms of order higher than n_{cutoff} will not contribute substantially to the nonlinear solution of (4.15) and it is not necessary to be included.

4.2.2 Numerical Approach

The proposed analytic solution assumes a linear dependance between the capacitance of the varactors and their applied voltage. This is however an ideal behavior. Consequently, if we want to model non-linear capacitance variations we have to follow a numerical approach. The discrete nature of the lattice favors a finite difference scheme in which the time derivatives are approximated by finite differences. The simplest approach is a two step calculation in which the lattice currents are intermediate variables.

Initially one 3-dimensional voltage and two (horizontal and vertical) 3-dimensional current matrices are defined:

$$\begin{aligned} &[V] = [V_{i,j,t}] \\ &[I^H] = [I^H_{i,j,t}] \\ &[I^V] = [I^V_{i,j,t}] \\ &i, j \in \{1, ..., N\} \quad t \in \{1, ..., N\}, \end{aligned} \tag{4.18}$$

where i,j are the indices of the node of the lattice and t is the index of a time frame.

Assuming:

- A function $C(V)$ representing the capacitance/voltage dependence of the varactors.
- Coil inductance L with resistance r.
- Time step dt.
- Offset varactor voltage value V_{off}.

Then the Kirchhoff laws of 4.3 can be numerically approximated by:

$$
\begin{aligned}
I^H_{i,j,t} &= (1 + dt\frac{r}{L})I^H_{i,j,t-1} + \frac{dt}{L}(V_{i,j-1,t-1} - V_{i,j,t-1}) \\
I^V_{i,j,t} &= (1 + dt\frac{r}{L})I^V_{i,j,t-1} + \frac{dt}{L}(V_{i-1,j,t-1} - V_{i,j,t-1}) \\
V_{i,j,t} &= V_{i,j,t-1} + \frac{dt(I^H_{i,j,t} + I^V_{i,j,t} - I^H_{i,j+1,t} - I^V_{i+1,j,t})}{C(V_{i,j,t-1} - V_{off})}
\end{aligned}
\tag{4.19}
$$

Initial knowledge of the voltage values at the lattice nodes is required in order for the numerical scheme to work. Without loss of generality these voltage values can be assumed to be zero.

4.3 Simulations

In order to verify theoretically the previous results, a two dimensional non-liner lattice with characteristics displayed in table 4.1, was considered.

The voltage inputs applied to this lattice are simple AC voltage sources with variable amplitude A and variable frequency ω_o. All of the inputs are in phase. In the frequency domain these inputs are represented by delta functions and are contained in the boundary vector $\{\hat{s}\}$:

$$
\begin{aligned}
\{\hat{s}\} &= \frac{A}{2}[\delta(\omega - \omega_o) + \delta(\omega + \omega_o)]\{s\} \\
\{s\} &= \{0_{N^2}, S^V_{1:N^2}, S^H_{1:N^2}\} \\
\{S^V_{1:N^2}\} &= \{0, 1_{1:N-1}, 0_{N(N-1)}\} \\
\{S^H_{1:N^2}\} &= \{0_N, 1, 0_{N-1}, 1, 0_{N-1}, ..., 0_{N-1}, 1\}
\end{aligned}
$$

Table 4.1: Parameters of the 20×20 lattice.

Inductance	$L = 380$ nH
Inductor resistance	$r = 0.461$ Ohm
Inductor tolerance	2%
Boundary termination resistance	$r_b = 57$ Ohm
Varactors	See Fig. 4.5
Varactor tolerance	5%
Nonlinear coefficient	$b = 0.2823$ V^{-1}
Constant capacitance	$C_o = 162$ pF.

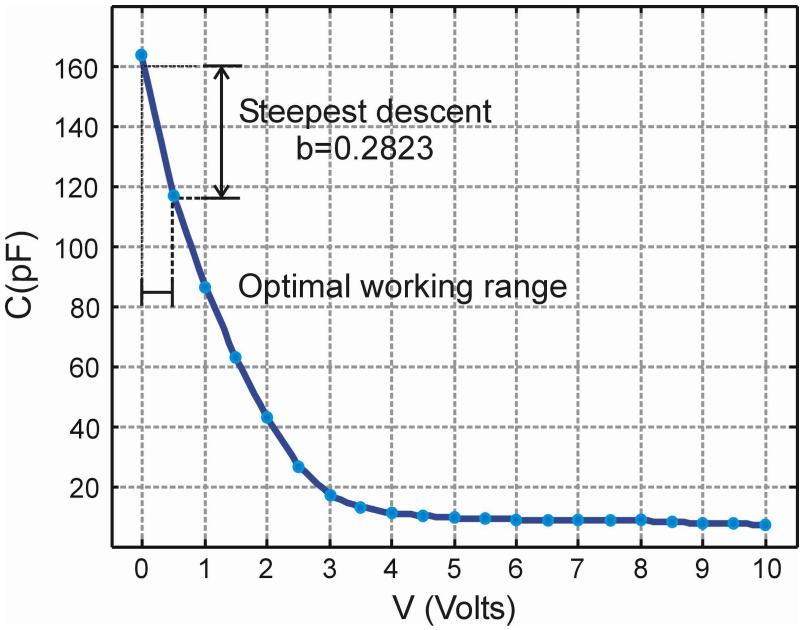

Figure 4.5: Capacitor C-V curve

(4.20)

Based on the varactor C-V plot the steepest descend interval is the interval [0,0.5] Volts and is characterized by a nonlinear coefficient $b = 0.2823$ according to (4.2). As it was determined experimentally, the optimal operating point is at $V_{off} = 200$ mV which is characterized by capacitance $C(V_{off}) = 144$ pF.

4.3.1 Lattice modal analysis

The specific lattice studied here, given that $L = 380$nH and $C(V_{off}) = 144$ pF has cutoff frequency according to (4.17) $f_{cutoff} = 60.838$MHz. Therefore, before studying the behavior of the non-linear lattice, an eigen-mode analysis is required in order to specify optimal operating frequencies. This analysis can be done by plotting the magnitude of the minimum eigenvalue of the matrix $[M(\omega)]$ in (4.16), as a function of the frequency $f = \frac{\omega}{2\pi}$. Such a plot for the lattice studied here is displayed in Fig. 4.6

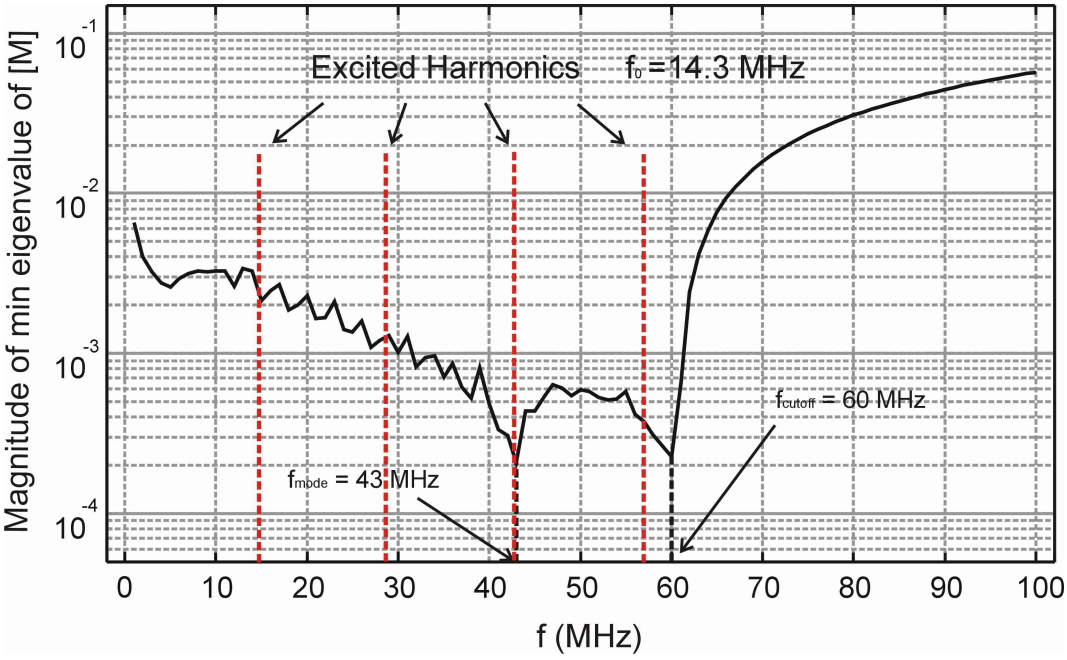

Figure 4.6: Eigen-mode analysis of the LC lattice

Based on Fig. 4.6 and in order to observe higher order harmonic amplification we have to excite the lattice at frequencies which have harmonics near the minima (modes) of Fig. 4.6. These minima appear at f_{mode} = 43MHz and f_{cutoff} = 60MHz. These modes are $\Delta f = 60 - 43 = 17$MHz apart. However an operating frequency at f_o = 17MHz is not going to excite them both since it will excite the frequencies $\{17, 34, 51, 68\}$MHz. A better choice choice for an operating frequency is at f_o = 14.3MHz. This frequency will excite the harmonics $\{14.3, 28.6, 42.9, 57.2\}$MHz of which the harmonic $42.9MHz$ is close to the mode f_{mode} = 43MHz and the harmonic 57.2MHz is close to the cutoff frequency mode f_{cutoff} = 60MHz. It is noteworthy to point out that these modes can be excited by high order harmonics of lower operating frequencies (Ideally, if the operating frequency was at f_o = 1 MHz all the modes of the lattice could have been excited). However in these cases the high order harmonics will be subsided by the effect of the coefficient b^k in the solution (4.11) when k is relatively large and $b < 1$.

4.3.2 Theoretical spectral analysis

In order to verify the above observations we simulated the behavior of the LC lattice mentioned previously using the proposed numerical scheme with in-phase sinusoidal sources of constant amplitude and variable frequency ranging from 1-70 MHz with 1 MHz step. The sources were located at the bottom and left side of the lattice as Fig. 4.4 displays. We plotted the magnitude of the fourier transform of the lattice response at the central node (9,9) for each driving frequency in a two dimensional plot displayed in Fig. 4.7.

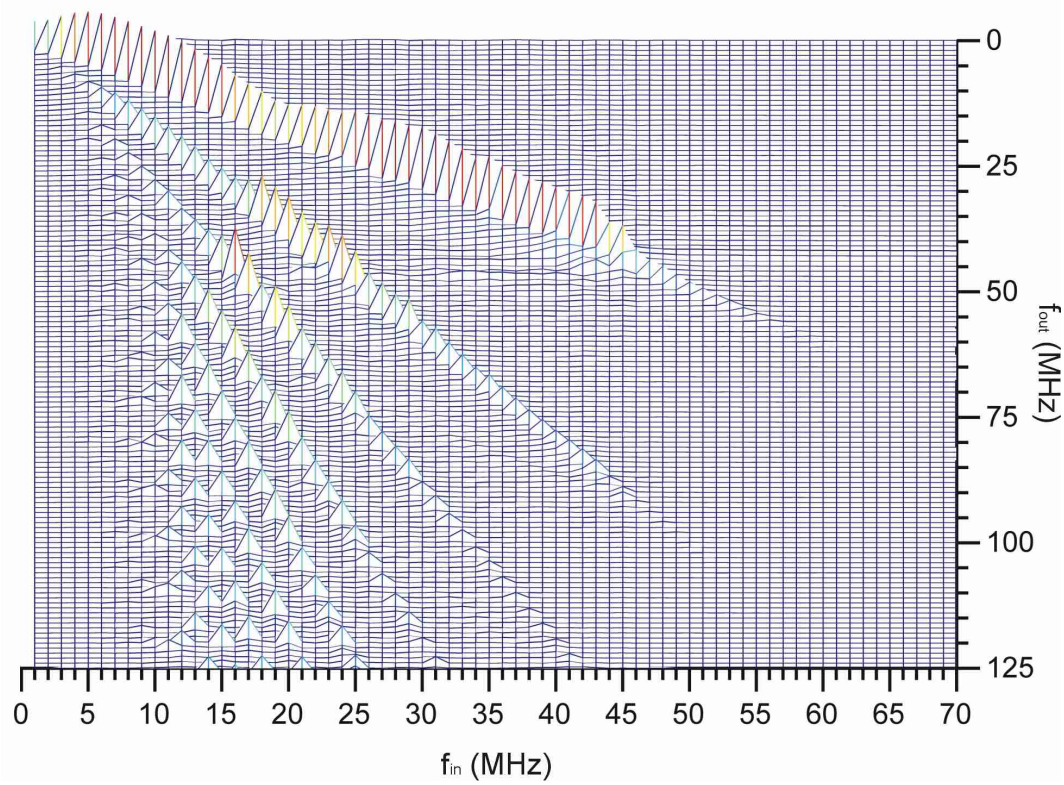

Figure 4.7: Theoretical spectral analysis of the LC lattice

Remarks

If the input and the output frequencies are treated as the x,y coordinates in a two dimensional cartesian map, then peak values of the plot of Fig. 4.7 appear at lines (rays) passing from the origin and satisfying $y = ax$. The most intense peaks appear in the $a = 1$ ray which constitutes the linear response of the lattice ($f_{in} = f_{out}$).

As it is expected and based on the theoretical results of Fig. 4.7 the nonlinear LC lattice amplify selectively the harmonics of a certain desirable frequency range. This range is between the input frequencies 10-25MHz. It is clear that in these frequencies part of the energy of the linear output of the lattice ($a = 1$ ray of the plot of Fig. 4.7) is used in order to amplify the higher order harmonics ($a > 1$ rays of the plot of Fig. 4.7)

Furthermore the lattice behaves linearly for input frequencies greater than 30MHz,

fact that is expected since the first harmonic of > 30 MHz (> 60 MHz) is considerably suppressed by the lattice cutoff frequency (plot of Fig. 4.6).

4.4 Experiments

A nonlinear two dimensional LC lattice with characteristics mentioned in the previous section was implemented on a PCB board. This lattice is displayed in Fig. 4.8

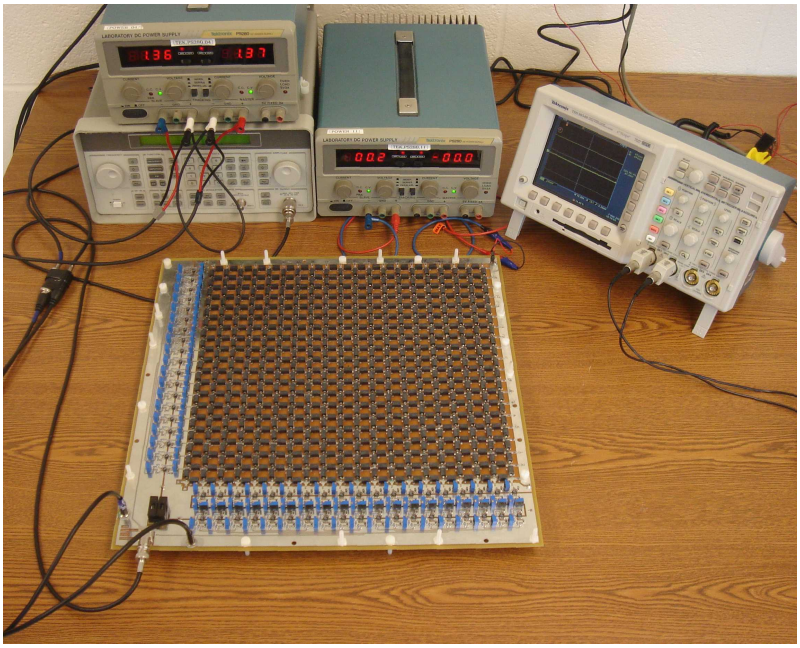

Figure 4.8: Photo of the LC lattice

The units which appear with blue color are the input voltage sources. Each one has a variable amplitude/phase capability. These voltage sources were applied at the nodes satisfying ($i = 1, 2 <= j <= 20$) and ($2 <= i <= 20$, $j = 1$) (refer to Fig. 4.1).

4.4.1 Voltage offset sweep

The first experiment one should perform in order to characterize the nonlinear behavior of the previous LC lattice is to specify the optimal varactor operating voltage. Looking at the C-V curve of Fig. 4.5 one can point out that there are voltage regions where the capacitance descent is steepest. The steeper capacitance descent is, the more intense the nonlinear harmonic generation is. This is due to the fact that steeper capacitance descent points are associated with higher b coefficient values (4.11) amplifying higher harmonics. In order to examine the point of the steepest descent the following simple experiment was performed.

All the varactors have to be biased at a negative V offset voltage. This can be accomplished by forcing all of their pins that are not connected to the coils of the lattice to have a constant negative DC voltage value - Voff. Setting the input peak to peak amplitude of all the sources at 1 volt we calculated the highest among all the lattice nodes peak to peak voltage value. This measurement was performed for different offset voltage values ranging from 25 to 500 mV. Since the input amplitude was kept at 1 V peak to peak, the observed maximum peak to peak values at the lattice nodes, are also the boost ratios for the respective V offset values defined by:

$$R_{boost} = \frac{\max_{i,j} V_{ij}^{p-p}}{V_{in}^{p-p}} \tag{4.21}$$

In (4.21) V_{ij}^{p-p} is the measured peak to peak voltage value at node i, j and V_{in}^{p-p} is the input peak to peak value.

The plot of Fig. 4.9 contains the measured boost ratios as a function of the varactor DC voltage offset value.

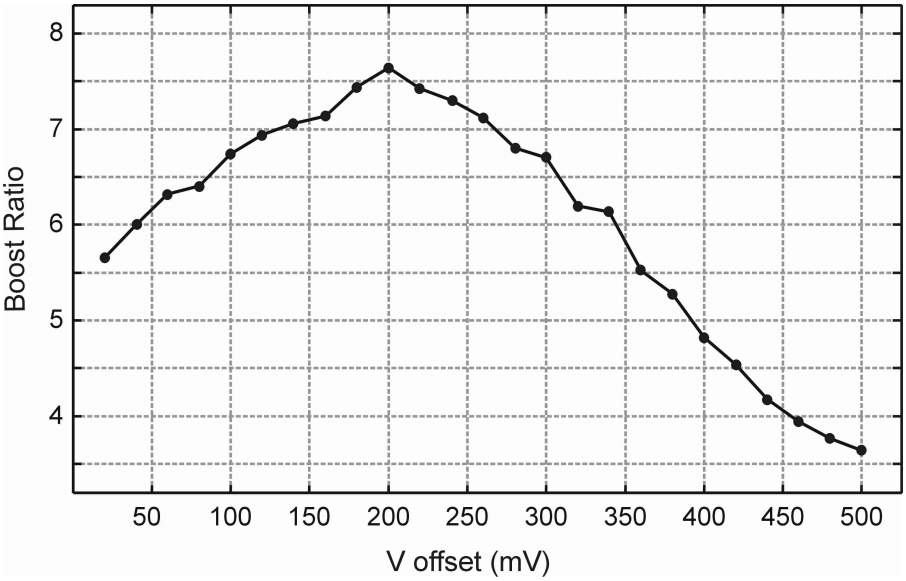

Figure 4.9: Boost ratios as a function of V offset voltage

Remarks

As it can be derived from the plot of Fig. 4.9 the optimal biasing V offset value is 200 mV. This value is at the close to the middle of the optimal $0 - 0.5$ V voltage range in which the steepest capacitance descent is observed (refer to the C-V curve of Fig. 4.5 which is provided by the manufacturer of the varactor diodes). For the rest of the experiments the varactor voltage offset value of 200mV was retained.

4.4.2 Input amplitude sweep

In order to find the point of greatest non-linear amplification as a function of the input peak to peak voltage, we calculated the greatest observed peak to peak value among all the nodes of the lattice. As it was expected based on symmetry arguments the highest peak to peak values were observed along the main diagonal of the lattice (nodes satisfying i=j). Calculating the ratios of the highest measured peak to peak voltage value over

the input peak to peak voltage, the boost ratios were derived according to (4.21). The plot of Fig. 4.10 displays the obtained boost ratios as a function of the input peak to peak value.

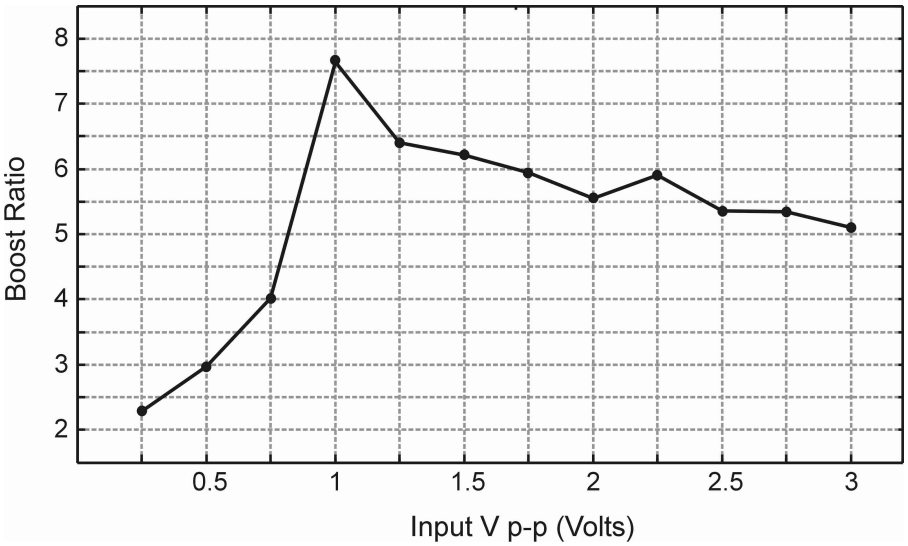

Figure 4.10: Boost ratios as a function of input peak to peak voltage

Remarks

The plot of Fig. 4.10 suggest that the optimal input peak to peak voltage value which will result to the highest non-linear boost ratio is 1 Volt. Therefore, for the rest of the experiments this optimal 1 Volt peak to peak input amplitude was retained.

4.4.3 Experimental spectral analysis

In order to characterize the behavior of the lattice and determine the optimal operating frequency, an experimental spectral analysis was performed. Sinusoidal voltage inputs of amplitude 1 V peak to peak were applied at the bottom and left side of the lattice (blue regions of Fig. 4.8). All the inputs were in phase. Their frequency varied from 1

to 70 MHz with 1 MHz step. We measured the responses at the central node $(9, 9)$ for each frequency. The magnitude of the fourier transform of each of the 70 obtained wave forms is displayed in the two dimensional plot of Fig. 4.11.

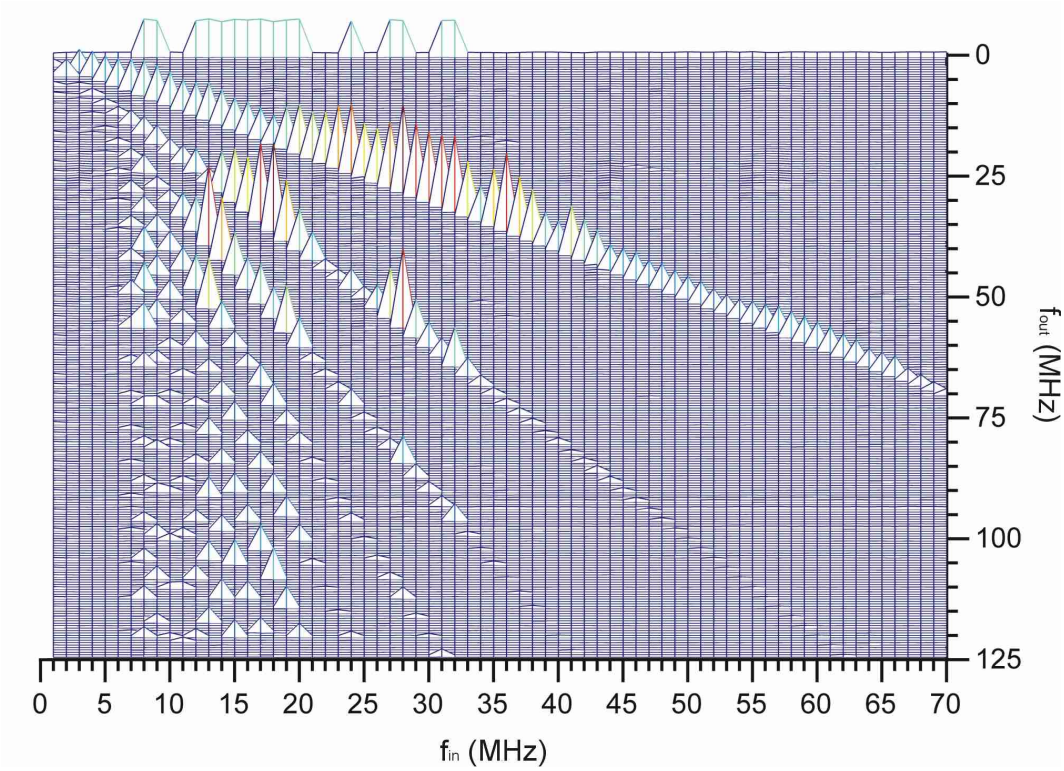

Figure 4.11: Experimental spectral analysis of the LC lattice

Remarks

The experimental results of Fig. 4.11 conform with the simulated ones in Fig. 4.7. There are however noteworthy differences.

The non-linear harmonic generation starts for input frequencies 7MHz as opposed to 10MHz which appear in the theoretic results. A possible reason for this inconsistency is the overestimated constant capacitance $C(V_{off}) = 144$pF. A possible lower real constant capacitance will force all the phenomena to appear in lower frequencies.

A DC output component appears at input frequencies which generate higher order

harmonics (range 10-35 MHhz). This phenomenon does not appear in the numerical simulation results. Based on the perturbation analysis this DC generation is expected as a result of the convolution operations appeared in (4.12).

4.4.4 Frequency sweep

In order to verify the results of the spectral analysis we plotted the maximum measured peak to peak voltage value as a function of the input frequency. Furthermore since the input amplitude was kept constant at 1 Volt peak to peak, these observed maximum peak to peak values, are equal with the lattice boost ratios. These measurements are displayed in the plot of Fig. 4.12.

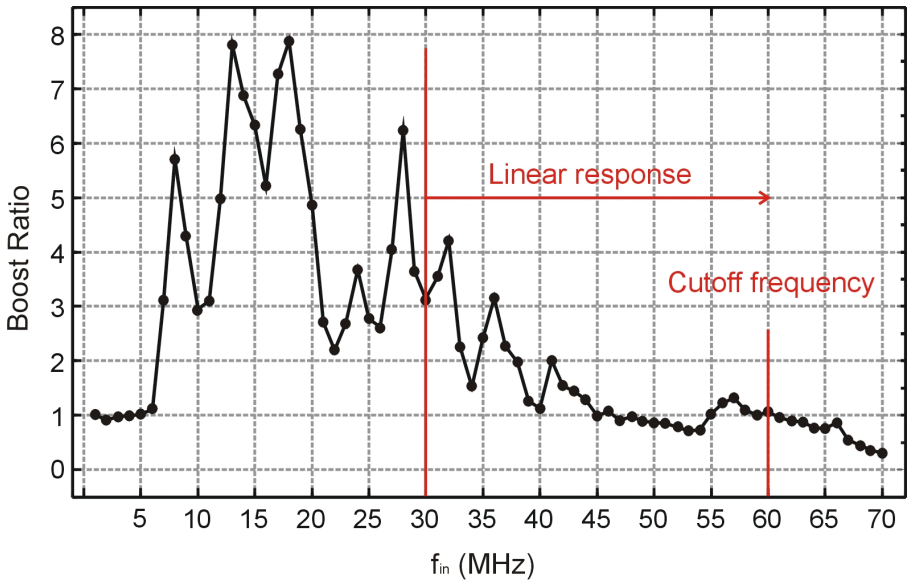

Figure 4.12: Boost ratios as a function of input frequency

Remarks

The experimental results of Fig. 4.12 agree with the conclusions of the eigenvalue analysis mentioned in section 4.3.1. Nonlinear amplification appear in frequencies $8, 13, 18, 28$ MHz with boost ratios greater than 5. Additionally, as the frequency increases, and for frequencies higher than 30 MHz the amplification becomes linear with boost ratios < 4.5. This is expected, since for fundamental frequencies higher than 30 MHz the excited higher order harmonics exceed the cutoff frequency bound of 60 MHz.

The amplification observed at frequency 13.5 Mhz can be explained by the excitation of both of the lattice modes: at 40-43Mhz (Fig. 4.6) by the third harmonic ($3 \times 13.5 = 40.5$MHz), and at 55-60 Mhz (Fig. 4.6) by the "near by" forth harmonic ($4 \times 13.5 = 54$Mhz). The effects of these excitations are added to the effects caused by the fundamental and the second harmonic. In this way the final amplification is maximized.

Additionally, the amplification observed at frequency 28 Mhz can be explained by the excitation of the lattice mode at 55-60Mhz (Fig. 4.6) by the second harmonic ($2 \times 28 = 56$MHz) which is added to the effect caused by the fundamental frequency. The effects generated by the third ($3 \times 28 = 84$MHz) or higher harmonics are subsided by the 61 Mhz cutoff frequency bound.

In the same way, the amplification observed at frequency 18.5 Mhz can be explained by the excitation of the lattice mode at 55-60 Mhz by the third harmonic ($3 \times 18.5 = 55.5$MHz), effect which is added to the contributions of the fundamental and the second harmonic.

The small peaks observed in the boot ration vs frequency plot of Fig. 4.12 at frequencies 42 Mhz and 57 Mhz are inside the intervals of the theoretically calculated

lattice modes (40-43Mhz and 55-60 Mhz in Fig. 4.6).

Finally, the cutoff frequency value calculated based on (4.17) ($\approx 61Mhz$) agrees with the experimental results of Fig. 4.12 since after 61 Mhz the boost ratio becomes smaller than 1. Based on these results, the operating frequency for the rest of the experiments was chosen to be 13.5 MHz.

4.4.5 Optimal results

Based on previous experimental measurements the optimal conditions at which the greatest nonlinear harmonic amplifications is observed are:

Input peak to peak amplitude $V_{p-p}^{in} = 1$ Volt.

Operating frequency $f_{in} = 13.5$MHz.

Varactor bias voltage $V_{bias} = 200$mV.

In these conditions the maximum voltage peak to peak value is obtained at the node (9,9). The waveform measured at node (9,9) is compared with the input waveform at node (1,10). Both waveforms are displayed in the left plot of Fig. 4.13. Their respective fourier transforms are displayed in the right plot of Fig.4.13.

Remarks

As Fig. 4.13 indicates, when the lattice operates at the optimal conditions the 3^{rd} (40.5MHz) and the 4^{th} harmonic (54MHz) of the input are significantly amplified. This fact conforms with our eigen-mode analysis discussed in section 4.3.1. Furthermore the harmonics $> 5^{th}$ are suppressed since they exceed the cutoff frequency of 61MHz.

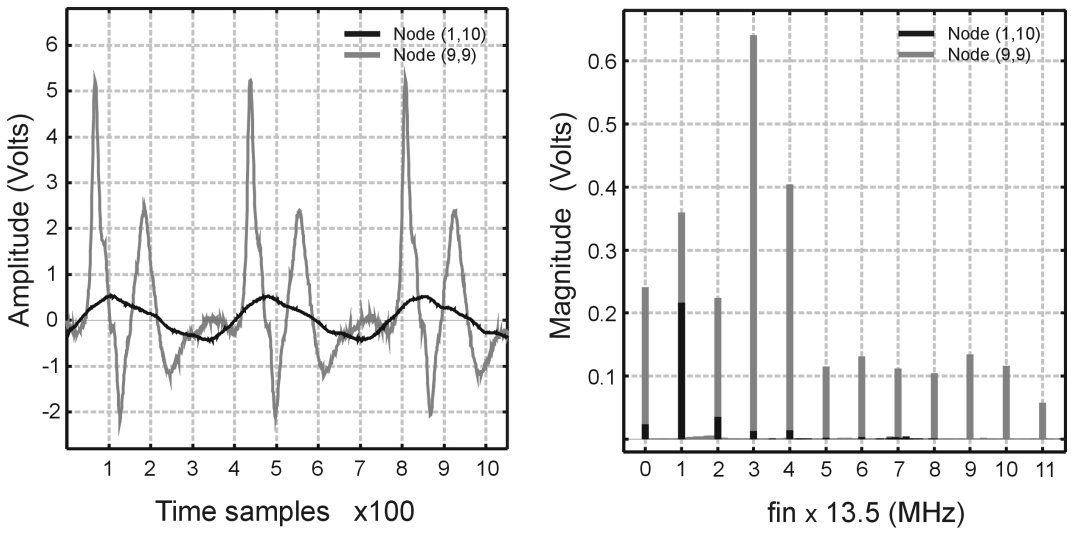

Figure 4.13: Output (Node (9,9)) vs. input (Node (1,10)). Left: Waveforms. Right: Fourier transforms.

4.4.6 Peak to peak voltage distribution

In order to study the intensity of the constructive interference at all of the lattice nodes, we plotted the measured peak to peak amplitude values at every node of the lattice. For this measurement we set the operating frequency at 13.5 Mhz and the input amplitude at 2 Volts peak to peak. The obtained measurements were compared with the theoretical ones obtained from a linear lattice (with $C = C(V_{off}) = 144pF$), having the same topology, same input and same operating frequency. Fig. 4.14 displays the peak to peak voltage distribution for the linear lattice (Left) and the Non-Linear lattice (Right).

Remarks

It is evident based on the plots of Fig. 4.14 that the amplitude amplification observed at the nonlinear lattice is higher than the amplification observed at its linear counterpart. Furthermore, the areas of the observed amplification are smaller in the nonlinear lattice than in the linear equivalent. This suggests that the amplification of the nonlinear lattice

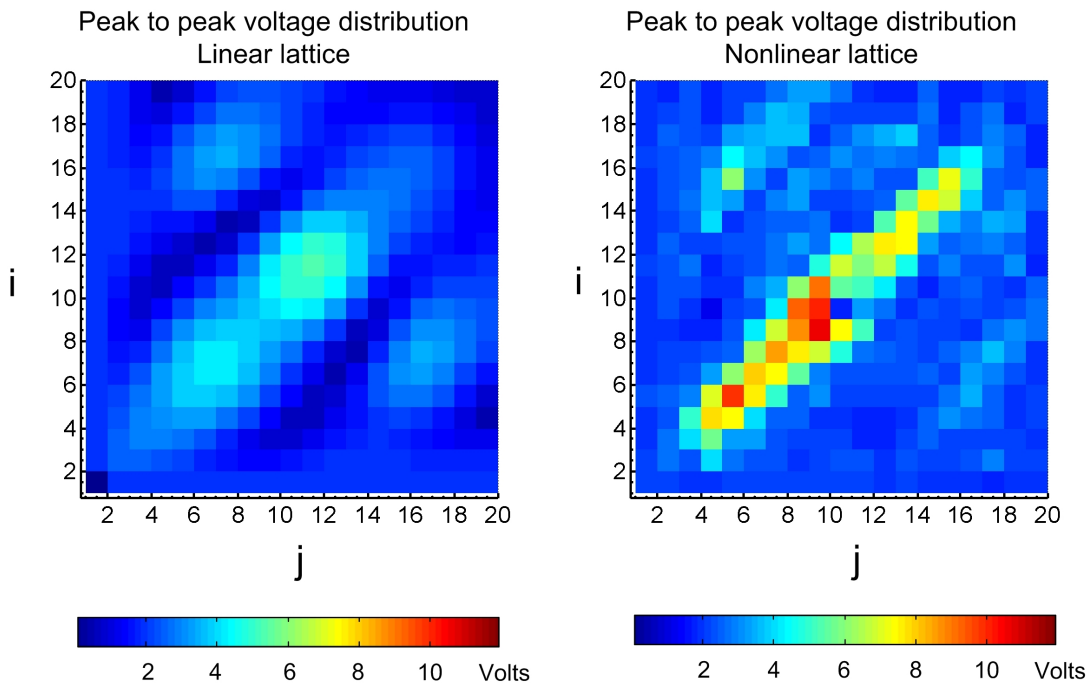

Figure 4.14: Peak to peak voltage values. **Left:** Linear lattice. **Right:** Non-linear Lattice.

is significantly localized. This amplification and localization observed in the nonlinear lattice compared with its linear equivalent can be explained from an energy conservation point of view. The input energy coming from the sine sources at the sides of the lattice is focused in the center nodes of the nonlinear lattice without being wide spread as it happens in its linear equivalent.

The results observed in the nonlinear lattice are not symmetrical with respect to the i=j diagonal nodes. This effect is caused by the non identical capacitance and inductance values (Based on the manufacturer's specifications inductor tolerance was 2% and varactor tolerance was 5 %).

4.5 Conclusions

It was verified using theoretical and experimental tools that when nonlinear LC lattices operate at optimal conditions they exhibit a rich nonlinear behavior characterized by high frequency harmonic generation and voltage amplification. These conditions can be specified by applying a sequence of tests starting from the optimal biasing voltage value of the varactors to the specification of the optimal input peak to peak amplitude and frequency operating points. Towards this direction a minimum eigenvalue plot (like the one in Fig. 4.6) and a varactor CV curve, can provide useful intuition about these optimal conditions.

CHAPTER 5

EPILOGUE

Wave fields could potentially be synthesized in every wave medium. In order for one to determine an efficient method of synthesizing wave fields, the knowledge of the wave propagation law, is essential.

As it was demonstrated in the second and third chapter of this thesis, when the wave medium behaves linearly, an optimal wave field synthesis method can be established. This method finds applications in multichannel sound systems achieving synthesis of acoustic wave fields and in antenna arrays providing synthesis of electromagnetic wave fields.

When the nature of medium is nonlinear such optimal wave field synthesis method is difficult to be determined. In this case approximate solution techniques give useful intuition about the nature of the synthesized fields. An example of nonlinear wave field synthesis was studied in the forth chapter where the behavior of a discrete two dimensional nonlinear LC electrical lattice was analyzed both theoretically and experimentally.

Generally the knowledge of effective wave field synthesis methods enables the designer to determine the appropriate source signals, given specific source locations, in order for the synthesis results to be the desirable ones. Furthermore, in the case of two dimensional nonlinear LC lattices, this knowledge gives also the appropriate tools for the design of devices capable of shaping wave fields, as well.

APPENDIX A

SYNTHESIS OF WAVE FIELDS USING POINT SOURCES

The goal of this appendix is to specify the optimal square integrable spectra $\hat{S}_j^{opt}(\omega) \in \mathcal{L}^2(\mathbf{R})$, satisfying $\hat{S}_j^{opt}(\omega) = \hat{S}_j^{*opt}(-\omega)\ \forall\omega \in \mathcal{R}$, which minimize the error given by:

$$E(\{\hat{S}(\omega)\}) = 2\int_S \left[\int_{\mathcal{R}} |\hat{P}_o(\vec{r},\omega) - \sum_j \hat{S}_j(\omega)G_j(\vec{r},\omega)|^2 d\omega\right] ds \tag{A.1}$$

where $\{\hat{S}(\omega)\} = \{\hat{S}_1(\omega), ..., \hat{S}_M(\omega)\}$.

Since the spectral distribution $\hat{P}_o(\vec{r},\omega)$ is assumed to be bandlimited inside a band Ω the error expression of (A.1) can be written as:

$$\begin{aligned} E(\{\hat{S}(\omega)\}) = \quad & 2\int_S \left[\int_{\Omega} |\hat{P}_o(\vec{r},\omega) - \sum_j \hat{S}_j(\omega)G_j(\vec{r},\omega)|^2 d\omega\right] ds + \\ & 2\int_S \left[\int_{\mathcal{R}/\Omega} |0 - \sum_j \hat{S}_j(\omega)G_j(\vec{r},\omega)|^2 d\omega\right] ds \end{aligned} \tag{A.2}$$

Our goal is to determine the optimal spectra $\hat{S}_j^{opt}(\omega)$ which minimize the above double integrals. Clearly since the last integral in the above equation is always positive, it follows that the optimal spectra $\hat{S}_j^{opt}(\omega)$ that minimize E must have support the interval Ω. In other words it must be $\hat{S}_j(\omega) = 0\ \forall\omega \in \mathcal{R}/\Omega$. After this conclusion the error $E(\{\hat{S}(\omega)\})$ is reduced to:

$$E(\{\hat{S}(\omega)\}) = 2\int_S \left[\int_{\Omega} |\hat{P}_o(\vec{r},\omega) - \sum_{j=1}^{M} \hat{S}_j(\omega)G_j(\vec{r},\omega)|^2 d\omega\right] ds \tag{A.3}$$

In the next two sections we define two classes of functions $\Sigma_n[\Omega]$,$n \in \mathcal{N}$ and $\mathcal{L}^2[\Omega]$ which will be used in the process of the minimization of $E(\{\hat{S}(\omega)\})$.

A.1 Synthesis in $\Sigma_n[\Omega]$, $n \in \mathcal{N}$

A.1.1 Class $\Sigma_n[\Omega]$, $n \in \mathcal{N}$ definition

Class $\Sigma_n[\Omega]$ is defined as the following set of simple functions:

$$\Sigma_n[\Omega] = \left\{ \hat{S} : \Omega \to C \quad \hat{S}(\omega) = \sum_{i=1}^{n} s_i I_{\Omega_i}(\omega) \right\} \tag{A.4}$$

with

$$I_{\Omega_i}(\omega) = \begin{cases} 1 & \omega \in \Omega_i \\ 0 & \omega \in \Omega / \Omega_i \end{cases} \tag{A.5}$$

$$\begin{aligned} & |s_i| < \infty \\ & \Omega_i = \left(2\pi(f_c - f_s) + 4\pi f_s \frac{(i-1)}{2^n}, 2\pi(f_c - f_s) + 4\pi f_s \frac{i}{2^n} \right] \\ & i \in \{1, ..., 2^n\} \end{aligned} \tag{A.6}$$

These classes are nested i.e.:

$$\Sigma_0[\Omega] \subset \Sigma_1[\Omega] \subset .... \subset \Sigma_\infty[\Omega] \tag{A.7}$$

A.1.2 Synthesis in $\Sigma_n[\Omega]$, $n \in \mathcal{N}$

In order to synthesize optimally wave fields with sources having $\Sigma_n[\Omega]$ spectra we have to find vector of functions $\{\hat{S}_n(\omega)\} = \{\hat{S}_{n1}(\omega), ..., \hat{S}_{nA}(\omega)\}$ with $\hat{S}_{nj}(\omega) \in \Sigma_n[\Omega]$, $j = 1, ..., M$ and $n \in \mathcal{N}$ such that the error in equation (A.3) is minimized. Equivalently we have to find:

$$\{\hat{S}_n(\omega)\}^{opt} = \arg \min_{\hat{S}_{nj}(\omega) \in \Sigma_n[\Omega]} \left[E(\{\hat{S}_n(\omega)\}) \right] \tag{A.8}$$

In order to solve the above minimization problem we have to restrict ourselves in the class of spectra $\hat{S}_{nj}(\omega) \in \Sigma_n$. In this case, the inner integral of the error expression of (A.3) becomes a sum of n integrals over each interval Ω_i that is defined in the class $\Sigma_n[\Omega]$ with $i \in \{1, ..., 2^n\}$:

$$E(\{\hat{S}_n(\omega)\}) = 2 \int_S \sum_{i=1}^{2^n} \left[\int_{\Omega_i} |\hat{P}_o(\vec{r}, \omega) - \sum_{j=1}^{M} \hat{S}_{nj}(\omega) G_j(\vec{r}, \omega)|^2 d\omega \right] ds \tag{A.9}$$

Now since $\hat{S}_{nj}(\omega) \in \Sigma_n[\Omega]$ the value of $\hat{S}_{nj}(\omega)$ is constant $\forall \omega \in \Omega_i$. Without loss of generality we can set:

$$\hat{S}_{nj}(\omega) = s_{ij} \in C \quad \forall \omega \in \Omega_i \quad j = \{1, ..., M\} \quad i = \{1, ..., 2^n\} \tag{A.10}$$

Based on the above notation the spectra $\hat{S}_{nj}(\omega) \in \Sigma_n[\Omega]$ can be written as:

$$\hat{S}_{nj}(\omega) = \sum_{i=1}^{2^n} S_{ij} I_{\Omega_i}(\omega) \tag{A.11}$$

Let us define the following vectors: $\{S_i\} = \{S_{i1}, ..., S_{iM}\}$. Based on this definition and according to (A.10) the error $E(\{\hat{S}_{nj}(\omega)\})$ becomes a function of the vectors $\{S_i\}$, $i = \{1, ..., 2^n\}$.

$$E(\{S_i\}) = 2 \int_S \sum_{i=1}^{2^n} \left[\int_{\Omega_i} |\hat{P}_o(\vec{r}, \omega) - \sum_{j=1}^{M} S_{ij} G_j(\vec{r}, \omega)|^2 d\omega \right] ds \tag{A.12}$$

Furthermore we can write the above error as a sum of positive error quantities $E(\{S_i\})$ that depend only of the vector $\{S_i\}$:

$$\begin{aligned} E(\{\hat{S}_n(\omega)\}) &= 2 \sum_{i=1}^{2^n} E(\{S_i\}) \\ E(\{S_i\}) &= \int_S \left[\int_{\Omega_i} |\hat{P}_o(\vec{r}, \omega) - \sum_{j=1}^{M} S_{ij} G_j(\vec{r}, \omega)|^2 d\omega \right] ds \end{aligned} \tag{A.13}$$

This inner integral of (A.13) can be written in a more convenient quadratic form as:

$$E(\{S_i\}) = [\{S_i\}^H [H_i] \{S_i\} + \{S_i\}^H \{l_i\} + \{l_i\}^H \{S_i\} + c_i] \tag{A.14}$$

where the matrix $[H_i]$, the vector $\{l_i\}$ and the constant c_i are defined by:

$$\begin{aligned} [H_i]_{pq} &= \int_S \left[\int_{\Omega_i} G_p(\vec{r}, \omega) G_q^*(\vec{r}, \omega) d\omega \right] ds \quad p, q \in \{1, ..., M\} \\ \{l_i\}_q &= \int_S \left[\int_{\Omega_i} \hat{P}_o(\vec{r}, \omega) G_q^*(\vec{r}, \omega) d\omega \right] ds \quad p \in \{1, ..., M\} \\ c_i &= \int_S \left[\int_{\Omega_i} |\hat{P}_o(\vec{r}, \omega)|^2 d\omega \right] ds \end{aligned} \tag{A.15}$$

According to equations (A.13) and (A.14) the error $E(\{S_i\})$ can be written as:

$$E(\{\hat{S}_n(\omega)\}) = 2\sum_{i=1}^{2^n} E(\{S_i\})$$
$$E(\{S_i\}) = \{S_i\}^H[H_i]\{S_i\} + \{S_i\}^H\{l_i\} + \{l_i\}^H\{S_i\} + c_i \tag{A.16}$$

As it is proven in section A.4 the quadratic $E(\{S_i\})$ obtains a minimum which is:

$$\min[E(\{S_i\})] = \left[c_i - \{l_i\}^H[H_i^{-1}]\{l_i\}\right] \tag{A.17}$$

when

$$\{S_i\}^{opt} = [H_i^{-1}]\{l_i\} \quad \forall i = \{1, ..., 2^n\} \tag{A.18}$$

Now based on equations (A.16) and (A.17) and the fact that $E(\{S_i\}) > 0$, $i = \{1, ..., 2^n\}$ it will be true that:

$$\min\left[E(\{\hat{S}_n(\omega)\})\right] = 2\sum_{i=1}^{2^n} \min[E(\{S_i\})]$$
$$\min\left[E(\{\hat{S}_n(\omega)\})\right] = 2\sum_{i=1}^{2^n} \left[c_i - \{l_i\}^H[H_i^{-1}]\{l_i\}\right] \tag{A.19}$$

Therefore the minimum of E will be obtained when:

$$\{S_i\}^{opt} = [H_i^{-1}]\{l_i\} \quad \forall i = \{1, ..., 2^n\} \tag{A.20}$$

or when

$$S_{ij}^{opt} = \sum_{q=1}^{A} [H_i^{-1}]_{jq} \{l_i\}_q \quad \forall i = \{1, ..., 2^n\} \tag{A.21}$$

Therefore we can conclude that the minimum of $E(\{\hat{S}_n(\omega)\})$ with $\{\hat{S}_n(\omega)\} = \{\hat{S}_{n1}(\omega), ..., \hat{S}_{nM}(\omega)\}$, $\hat{S}_{nj}(\omega) \in \Sigma_n[\Omega]$ is obtained when equation (A.21) is satisfied or when the spectra $\hat{S}_{nj}(\omega)$ according to (A.11) are given by:

$$\hat{S}_{nj}^{opt}(\omega) = \sum_{i=1}^{2^n} \left[\sum_{q=1}^{M} [H_i^{-1}]_{jq} \{l_i\}_q \right] I_{\Omega_i}(\omega) \tag{A.22}$$

with

$$\begin{aligned} [H_i]_{pq} &= \int_S \left[\int_{\Omega_i} G_p(\vec{r}, \omega) G_q^*(\vec{r}, \omega) d\omega \right] ds \quad p, q \in \{1, ..., M\} \\ \{l_i\}_q &= \int_S \left[\int_{\Omega_i} \hat{P}_o(\vec{r}, \omega) G_q^*(\vec{r}, \omega) d\omega \right] ds \quad p \in \{1, ..., M\} \end{aligned} \tag{A.23}$$

A.2 Synthesis in Σ_∞

Given the fact that the optimal spectra $\hat{S}_{jn}(\omega) \in \Sigma_n$ which minimize the square synthesis error are given by (A.22) we would like to calculate the limit of all these optimal solutions as $n \to \infty$. Equivalently we wish to calculate:

$$\hat{S}_j^{opt}(\omega) = \lim_{n \to \infty} \hat{S}_{jn}^{opt}(\omega) \tag{A.24}$$

or based on (A.22):

$$\hat{S}_j^{opt}(\omega) = \lim_{n\to\infty}\left[\sum_{i=1}^{2^n}\left[\sum_{q=1}^{M}[H_i^{-1}]_{jq}\{l_i\}_q\right]I_{\Omega_i}(\omega)\right] \tag{A.25}$$

The functions $\hat{P}_o(\vec{r},\omega)$ and $G_j(\vec{r},\omega)$, $j = 1,...,M$ are continuous and bounded with respect to ω. Our goal is to show that the limit of (A.25) converges to the following function:

$$\hat{S}_j^{opt}(\omega) = \sum_{q=1}^{M}[H(\omega)^{-1}]_{jq}\{l(\omega)\}_q \tag{A.26}$$

with

$$\begin{aligned}[H(\omega)]_{pq} &= \int_S [G_p(\vec{r},\omega)G_q^*(\vec{r},\omega)]ds \quad p,q \in \{1,...,M\}\\ \{l(\omega)\}_q &= \int_S [\hat{P}_o(\vec{r},\omega)G_q^*(\vec{r},\omega)]ds \quad p \in \{1,...,M\}\end{aligned} \tag{A.27}$$

In order to show that the limit of (A.25) converges to the function in equation (A.26) we first have to show that $\forall\omega_o \in \Omega$:

$$\forall e > 0 \;\; \exists N \in \mathcal{N} : \;\; n > N \Rightarrow |\hat{S}_{jn}^{opt}(\omega_o) - \hat{S}_j^{opt}(\omega_o)| < e \tag{A.28}$$

Lets define the difference:

$$\Delta\hat{S}_{nj}^{opt}(\omega) = \hat{S}_{nj}^{opt}(\omega) - \hat{S}_j^{opt}(\omega) \tag{A.29}$$

Assuming that the inverse of the matrix $[H(\omega)]_{pq}$ of (A.26) exists for every $\omega \in \Omega$ then the difference $\Delta\hat{S}_{nj}^{opt}(\omega)$ can be written as:

$$\Delta\hat{S}_{nj}^{opt}(\omega) = \sum_{i=1}^{2^n} \frac{\sum_{l=1}^{M!} \prod_{m=1}^{M} n_{lm}}{\sum_{q=1}^{M!} \prod_{r=1}^{M} d_{qr}} I_{\Omega_i} - \frac{\sum_{l=1}^{M!} \prod_{m=1}^{M} N_{lm}(\omega)}{\sum_{q=1}^{M!} \prod_{r=1}^{M} D_{qr}(\omega)} \tag{A.30}$$

with

$$\begin{aligned} & N_{lm}(\omega), D_{qr}(\omega) \in \left\{ \pm[H(\omega)]_{pq}, \{l(\omega)\}_q, p, q = 1, ..., M \right\} \\ & n_{lm} = \int_{\Omega_i} N_{lm}(\omega) d\omega \\ & d_{qr} = \int_{\Omega_i} D_{qr}(\omega) d\omega \end{aligned} \tag{A.31}$$

Let us consider a random $\omega_o \in \Omega$. There there exist an interval Ω_k, $k \in \{1, ..., 2^n\}$ for every $n \in \mathcal{N}$, such that $\omega_o \in \Omega_k$. Since the functions N_{lm}, D_{qr} are all continuous with respect to ω we can apply Rolle's in Ω_k which will give us that there exists $\omega_{lm}, \omega_{qr} \in \Omega_k$ such that:

$$\begin{aligned} n_{lm} &= \int_{\Omega_k} N_{lm}(\omega) d\omega = N_{lm}(\omega_{lm}) \mu(\Omega_k) \\ d_{qr} &= \int_{\Omega_k} D_{qr}(\omega) d\omega = D_{qr}(\omega_{qr}) \mu(\Omega_k) \end{aligned} \tag{A.32}$$

with $\mu(\Omega_k)$ being the total length (measure) of the interval Ω_k.

Now based on (A.30) and (A.32) we will have that:

$$|\Delta\hat{S}_{jn}^{opt}(\omega_o)| = \left| \frac{\sum_{l=1}^{M!} \prod_{m=1}^{M} N_{lm}(\omega_{lm})}{\sum_{q=1}^{M!} \prod_{r=1}^{M} D_{qr}(\omega_{qr})} - \frac{\sum_{l=1}^{M!} \prod_{m=1}^{M} N_{lm}(\omega_o)}{\sum_{q=1}^{M!} \prod_{r=1}^{M} D_{qr}(\omega_o)} \right| \tag{A.33}$$

or:

$$|\Delta\hat{S}_{jn}^{opt}(\omega_o)| = \frac{1}{|D_o||D_i|}\sum_{l,q=1}^{M!}|\Delta x_{lq}|$$
$$\Delta x_{lq} = \prod_{m,r=1}^{M} N_{lm}(\omega_{lm})D_{qr}(\omega_o) - \prod_{m,r=1}^{M} N_{lm}(\omega_o)D_{qr}(\omega_{qr}) \tag{A.34}$$

with the denominators D_o, D_i equal to the following determinants:

$$D_o = \det[H] = \sum_{q=1}^{M!}\prod_{r=1}^{M} D_{qr}(\omega_o)$$
$$D_i = \det[H_i] = \sum_{q=1}^{M!}\prod_{r=1}^{M} D_{qr}(\omega_{qr}) \tag{A.35}$$

If we set $\Delta N_{lm} = N_{lm}(\omega_{lm}) - N_{lm}(\omega_o)$ and $\Delta D_{qr} = D_{qr}(\omega_{qr}) - D_{qr}(\omega_o)$ then:

$$|\Delta\hat{S}_{jn}^{opt}(\omega_o)| = \frac{1}{|D_o||D_o + \delta D_o|}\sum_{l,q=1}^{M!}|\Delta x_{lq}|$$
$$\Delta x_{lq} = \prod_{m,r=1}^{M}[\Delta N_{lm} + N_{lm}(\omega_o)]D_{qr}(\omega_o) - \prod_{m,r=1}^{M} N_{lm}(\omega_o)[\Delta D_{qr} + D_{qr}(\omega_o)] \tag{A.36}$$

where the determinant D_i is equal to:

$$D_i = D_o + \delta D_o$$
$$D_i = \sum_{q=1}^{M!}\prod_{r=1}^{M}[D_{qr}(\omega_o) + \Delta D_{qr}]$$

$$D_i = \sum_{q=1}^{M!} \prod_{r=1}^{M} D_{qr}(\omega_o) + \sum_{q=1}^{M!} \prod_{r\neq s}^{M} D_{qr}(\omega_o)\Delta D_{qs}$$
$$\delta D_o = \sum_{q=1}^{M!} \prod_{r\neq s}^{M} D_{qr}(\omega_o)\Delta D_{qs} \tag{A.37}$$

After some eliminations we will obtain:

$$|\Delta \hat{S}_{nj}^{opt}(\omega_o)| = \frac{1}{|D_o||D_o + \delta D_o|} \sum_{l,q=1}^{M!} |\Delta s_{lq}| \quad \forall n \in \mathcal{N}$$
$$\Delta s_{lq} = \prod_{m,r=1}^{M} \Delta N_{lm} D_{qr}(\omega_o) - \prod_{m,r=1}^{M} \Delta D_{qr} N_{lm}(\omega_o) \tag{A.38}$$

Since the inverse of $[H(\omega)]^{-1}$ in (A.26) exists for all $\omega \in \Omega$ we will have that $|D_o| = \det[H] \neq 0$. Using the triangular inequality on (A.38) we obtain:

$$|\Delta \hat{S}_{nj}^{opt}(\omega_o)| < \frac{\sum_{l,q=1}^{M!} \prod_{m,r=1}^{M} |D_{qr}(\omega_o)||\Delta N_{lm}|}{|D_o|||D_o| - |\delta D_o||} + \frac{\sum_{l,q=1}^{M!} \prod_{m,r=1}^{M} |N_{lm}(\omega_o)||\Delta D_{qr}|}{|D_o|||D_o| - |\delta D_o||} \tag{A.39}$$

Furthermore, since the functions N_{nm} and D_{qr} are continuous and bounded in Ω it will be true that $\forall e_1 > 0 \;\; \exists N \in \mathcal{N}$ such that $\forall n > N$:

$$|\Delta N_{lm}| = |N_{lm}(\omega_{lm}) - N_{nm}(\omega_o)| < e_1$$
$$|\Delta D_{qr}| = |N_{qr}(\omega_{qr}) - N_{qr}(\omega_o)| < e_1$$
$$\exists P > 0 \;\; \max\left[|N_{lm}(\omega_o)|, |D_{qr}(\omega_o)|\right] < P$$
$$\omega_{lm}, \omega_{qr}, \omega_o \in \Omega_k \tag{A.40}$$

Based on the above bounds we have that for sufficiently small $e_1 > 0$ $\exists L > 0$ such that:

$$
\begin{aligned}
|\delta D_o| &= \left| \sum_{q=1}^{M!} \prod_{r \neq s}^{M} D_{qr}(\omega_o) \Delta D_{qs} \right| \leq M! \sum_{k=1}^{M} \begin{pmatrix} M \\ k \end{pmatrix} e_1^k P^{M-k} \\
|\delta D_o| &\leq e_1 \left[M! \sum_{k=1}^{M} \begin{pmatrix} M \\ k \end{pmatrix} e_1^{k-1} P^{M-k} \right] \\
L &\leq ||D_o| - |\delta D_o|| \\
L &= \left| |D_o| - e_1 \left[M! \sum_{k=1}^{M} \begin{pmatrix} M \\ k \end{pmatrix} e_1^{k-1} P^{M-k} \right] \right|
\end{aligned}
\tag{A.41}
$$

Inequality (A.39) given the bounds of (A.40) and (A.41) becomes:

$$
|\Delta \hat{S}_{nj}^{opt}(\omega_o)| < e_1^M \frac{2M! P^M}{|D_o| L} \tag{A.42}
$$

If we set

$$
e = e_1^M \frac{2M! P^M}{|D_o| L} \tag{A.43}
$$

then we have just showed that $\forall e > 0 \;\; \exists N \in \mathcal{N}$ such that $\forall n > N$:

$$
|\Delta \hat{S}_{nj}^{opt}(\omega_o)| = |\hat{S}_{nj}^{opt}(\omega) - \hat{S}_{j}^{opt}(\omega)| < e \tag{A.44}
$$

A.3 Synthesis in $\mathcal{L}^2[\Omega]$

A.3.1 Class $\mathcal{L}^2[\Omega]$ definition

Class $\mathcal{L}^2[\Omega]$ is defined as the following set of all square integrable functions with domain the set $[\Omega]$:

$$\mathcal{L}^2[\Omega] = \left\{ \hat{S} : \Omega \to C \quad \exists M > 0 : \int_{\Omega} |\hat{S}(\omega)|^2 d\omega < M \right\} \tag{A.45}$$

A.3.2 Density of $\Sigma_n[\Omega]$ in $\mathcal{L}^2[\Omega]$

It is obvious that $\Sigma_n[\Omega] \subset \mathcal{L}^2[\Omega]$ $\forall n \in \mathcal{N}$. Furthermore the set $\mathcal{L}^2[\Omega]$ is dense in $\Sigma_n[\Omega]$ according to the following lemma [30]:

Density lemma

For all $e > 0$ if $\hat{S}(\omega) \in \mathcal{L}^2[\Omega]$ exists a simple function $\hat{S}_n(\omega) \in \Sigma_n$ such that: $\|\hat{S} - \hat{S}_n\|_2 < e$ and $n \in \mathcal{N}$.

A.3.3 Error Convergence Lemma

Lets consider the error expression in (A.3), for functions $\hat{S}_{nj}(\omega) \in \Sigma_n$ that are e far from a function $\hat{S}_j(\omega) \in \mathcal{L}^2[\Omega]$.

$$E(\{\hat{S}_n(\omega)\}) = 2\int_S \int_\Omega E_n(\vec{r},\omega)d\omega ds$$
$$E_n(\vec{r},\omega) = \left| G(\vec{r}-\vec{r}_o) - \sum_{j=1}^{M} \hat{S}_{nj}(\omega) G(\vec{r}-\vec{r}_j) \right|^2 \tag{A.46}$$

The goal of this section is to prove the following error convergence lemma.

Error Convergence lemma

For every spectrum $\hat{S}_j(\omega) \in \mathcal{L}^2[\Omega]$ there exist spectrum $\hat{S}_{nj}(\omega) \in \Sigma_n[\Omega]$ such that $\forall e > 0$:

$$\sqrt{\int_\Omega |\hat{S}_j(\omega) - \hat{S}_{nj}(\omega)|^2 d\omega} < e \quad \forall j \in \{1, ..., M\} \tag{A.47}$$

and

$$|E(\{\hat{S}(\omega)\}) - E(\{\hat{S}_n(\omega)\})| \leq C(e) \tag{A.48}$$

with

$$C(e) = 2P\mu(S)[M^2 e + 2M\sqrt{\mu(\Omega)}]e \tag{A.49}$$

with $\mu(S)$, $\mu(\Omega)$ the measures of the medium S and the bandwidth Ω and $P > 0$.

The existence of an e distant sequence $\{\hat{S}_{nj}(\omega)\}$ is guaranteed by the density lemma. In order to prove this error convergence lemma we define:

$$\Delta\hat{S}_{nj}(\omega) = \hat{S}_{j}(\omega) - \hat{S}_{nj}(\omega) \tag{A.50}$$

Then equation (A.3) according to (A.50) becomes:

$$\begin{aligned} E(\{\hat{S}(\omega)\}) &= 2\int_S \int_\Omega E(\vec{r},\omega)d\omega ds \\ E(\vec{r},\omega) &= \left|\hat{P}_o(\vec{r},\omega) - \sum_{j=1}^{M}[\hat{S}_{j}(\omega)]G_j(\vec{r},\omega)\right|^2 \\ E(\vec{r},\omega) &= \left|\hat{P}_o(\vec{r},\omega) - \sum_{j=1}^{M}[\hat{S}_{nj}(\omega) + \Delta\hat{S}_{nj}(\omega)]G_j(\vec{r},\omega)\right|^2 \end{aligned} \tag{A.51}$$

Now based on (A.46) and (A.51) we can relate the quantities $E_n(\vec{r},\omega)$ and $E(\vec{r},\omega)$ using:

$$\begin{aligned} \Delta E_n(\vec{r},\omega) = \quad & E(\vec{r},\omega) - E_n(\vec{r},\omega) \\ \Delta E_n(\vec{r},\omega) = \quad & \left[\sum_{j=1}^{M}\Delta\hat{S}_{nj}(\omega)G_j(\vec{r},\omega)\right]\left[\sum_{j=1}^{M}\Delta\hat{S}^*_{nj}(\omega)G^*_j(\vec{r},\omega)\right] - \\ & \left[\hat{P}_o(\vec{r},\omega) - \sum_{j=1}^{M}\hat{S}_{nj}(\omega)G(\vec{r}-\vec{r}_j)\right]\sum_{j=1}^{M}[\Delta\hat{S}^*_{nj}(\omega)]G^*_j(\vec{r},\omega) - \\ & \left[\hat{P}^*_o(\vec{r},\omega) - \sum_{j=1}^{M}\hat{S}^*_{nj}(\omega)G^*_j(\vec{r},\omega)\right]\sum_{j=1}^{M}[\Delta\hat{S}_{nj}(\omega)]G_j(\vec{r},\omega) \end{aligned} \tag{A.52}$$

Essentially based on equations (A.46) (A.51) (A.52) we have:

$$|E(\{\hat{S}_j(\omega)\}) - E(\{\hat{S}_{nj}(\omega)\})| = 2\left|\int_S \int_\Omega \Delta E_n(\vec{r},\omega)d\omega ds\right| \tag{A.53}$$

Consider the functions:

$$\begin{aligned} K_{ij}(\vec{r},\omega) &= G_i(\vec{r},\omega)G_j^*(\vec{r},\omega) \\ L_j(\vec{r},\omega) &= \left[\hat{P}_o(\vec{r},\omega) - \sum_{k=1}^{M} \hat{S}_{nk}(\omega)G_k(\vec{r},\omega)\right] G_j^*(\vec{r},\omega) \end{aligned} \tag{A.54}$$

Furthermore, based on these functions $\Delta E_n(\vec{r},\omega)$ takes the form of:

$$\begin{aligned} \Delta E_n(\vec{r},\omega) = \quad & \left[\sum_{i,j=1}^{M} K_{ij}(\vec{r},\omega)\Delta\hat{S}_{ni}(\omega)\Delta\hat{S}_{nj}^*(\omega)\right] - \\ & \left[\sum_{j=1}^{M} L_j(\vec{r},\omega)\Delta\hat{S}_{nj}^*(\omega)\right] - \left[\sum_{j=1}^{M} L_j^*(\vec{r},\omega)\Delta\hat{S}_{nj}(\omega)\right] \end{aligned} \tag{A.55}$$

Since the domain S does not include the singular points of the functions $G_j(\vec{r},\omega)$, the K, L functions are bounded in the set $S \times \Omega$ and all the simple functions $\hat{S}_{nj}(\omega)$ are also bounded. In other words:

$$\exists P > 0 \quad max\left[|K_{ij}(\vec{r},\omega)|, |L_j(\vec{r},\omega)|\right] < P \tag{A.56}$$

Applying the triangular inequality on $\Delta E_n(\vec{r},\omega)$ in (A.55):

$$\begin{aligned} |\Delta E_n(\vec{r},\omega)| \leq \quad & \left[\sum_{i,j=1}^{M} |K_{ij}(\vec{r},\omega)||\Delta\hat{S}_{ni}(\omega)\Delta\hat{S}_{nj}^*(\omega)|\right] + \\ & \left[\sum_{j=1}^{M} |L_j(\vec{r},\omega)||\Delta\hat{S}_{nj}^*(\omega)|\right] + \left[\sum_{j=1}^{M} |L_j^*(\vec{r},\omega)||\Delta\hat{S}_{nj}(\omega)|\right] \end{aligned} \tag{A.57}$$

The last equation given the bounds of (A.56) and the fact that $|x^*| = |x| \forall x \in C$ becomes:

$$|\Delta E_n(\vec{r}, \omega)| \leq P \sum_{i,j=1}^{M} |\Delta \hat{S}_{ni}(\omega) \Delta \hat{S}_{nj}(\omega)| + 2P \sum_{j=1}^{M} |\Delta \hat{S}_{nj}(\omega)| \tag{A.58}$$

Application of the triangular inequality on equation (A.53) yields:

$$|E(\{\hat{S}_j(\omega)\}) - E(\{\hat{S}_{nj}(\omega)\})| \leq 2 \int_S \int_\Omega |\Delta E_n(\vec{r}, \omega)| d\omega ds \tag{A.59}$$

The last inequality given (A.58) becomes:

$$\begin{aligned} |E(\{\hat{S}_j(\omega)\}) - E(\{\hat{S}_{nj}(\omega)\})| \leq \quad & 2P\mu(S) \sum_{i,j=1}^{M} \int_\Omega |\Delta \hat{S}_{ni}(\omega) \Delta \hat{S}_{nj}(\omega)| d\omega + \\ & 4P\mu(S) \sum_{j=1}^{M} \int_\Omega |\Delta \hat{S}_{nj}(\omega)| d\omega, \end{aligned} \tag{A.60}$$

with $\mu(S) = \int_S ds$ being the measure of the medium.

Based on the definition of $\Delta \hat{S}_{nj}(\omega)$ in (A.50) we can write equation (A.47) as:

$$\sqrt{\int_\Omega |\Delta \hat{S}_{nj}(\omega)|^2 d\omega} < \epsilon \quad \forall j \in \{1, ..., M\} \tag{A.61}$$

Making use of the Schwartz inequality we can write:

$$\int_\Omega |\Delta \hat{S}_{ni}(\omega) \Delta \hat{S}_{nj}(\omega)| d\omega \leq \sqrt{\int_\Omega |\Delta \hat{S}_{ni}(\omega)|^2 d\omega \int_\Omega |\Delta \hat{S}_{nj}(\omega)|^2 d\omega} \tag{A.62}$$

Based on (A.61) equation (A.62) can be written as:

$$\int_{\Omega} |\Delta\hat{S}_{ni}(\omega)\Delta\hat{S}_{nj}(\omega)|d\omega \leq e^2 \quad \forall i, j \in \{1, ..., M\} \tag{A.63}$$

Substituting $\Delta\hat{S}_{ni}(\omega) = I_{\Omega}(\omega)$ in (A.62) will result to:

$$\int_{\Omega} |\Delta\hat{S}_{nj}(\omega)|d\omega \leq \sqrt{\mu(\Omega)} \sqrt{\int_{\Omega} |\Delta\hat{S}_{nj}(\omega)|^2 d\omega}, \tag{A.64}$$

with $\mu(\Omega)$ being the measure (length) of the bandwidth Ω.

Using again (A.61) the last inequality becomes:

$$\int_{\Omega} |\Delta\hat{S}_{nj}(\omega)|d\omega \leq e\sqrt{\mu(\Omega)} \quad \forall j \in \{1, ..., M\} \tag{A.65}$$

Inequality (A.60) based on inequalities (A.63) and (A.65) becomes:

$$|E(\{\hat{S}(\omega)\}) - E(\{\hat{S}_n(\omega)\})| \leq 2P\mu(S)\left[M^2e^2 + 2Me\sqrt{\mu(\Omega)}\right] \tag{A.66}$$

Or

$$|E(\{\hat{S}(\omega)\}) - E(\{\hat{S}_n(\omega)\})| \leq C(e), \tag{A.67}$$

with

$$C(e) = 2P\mu(S)\left[M^2e + 2M\sqrt{\mu(\Omega)}\right]e \tag{A.68}$$

A.3.4 Synthesis in $\mathcal{L}^2[\Omega]$

The goal of this sections is to specify functions $\hat{S}_j(\omega) \in \mathcal{L}^2[\Omega]$ $j = 1, ..., M$ contained in a vector $\{\hat{S}(\omega)\} = \{\hat{S}_1(\omega), \ldots, \hat{S}_M(\omega)\}$ such that the error in equation (A.3) is minimized. Equivalently we have to find:

$$\{\hat{S}(\omega)\}^{opt} = \arg \min_{\hat{S}_j(\omega) \in \mathcal{L}^2[\Omega]} \left[E(\{\hat{S}(\omega)\}) \right] \tag{A.69}$$

Contradiction is used in order to show that the solution to the above optimization problem is given by equation (A.26). Let's assume for the moment that the optimal spectra $\hat{S}_j^{\mathcal{L}^2 opt}(\omega) \in \mathcal{L}^2[\Omega]$, $j = 1, ..., M$ are not the spectra $\hat{S}_j^{opt}(\omega) \in \Sigma_\infty[\Omega]$, $j = 1, ..., M$ given by (A.26).

Based on the solution of (A.26) we know that:

$$E(\{\hat{S}^{opt}(\omega)\}) = \min_{\hat{S}_j(\omega) \in \Sigma_\infty[\Omega]} \left[E(\{\hat{S}(\omega)\}) \right] \tag{A.70}$$

Since the error E is always positive and because the optimal spectra $\hat{S}_j^{\mathcal{L}^2 opt}(\omega) \in \mathcal{L}^2[\Omega]$, $j = 1, ..., M$ are different from the spectra $\hat{S}_j^{opt}(\omega) \in \Sigma_n[\Omega]$ given by (A.26), and because $\Sigma_\infty[\Omega] \subset \mathcal{L}^2[\Omega]$, we can write that:

$$\exists \delta > 0 : \quad E(\{\hat{S}^{opt}(\omega)\}) = E(\{\hat{S}^{\mathcal{L}^2 opt}(\omega)\}) + \delta \tag{A.71}$$

Based on the error convergence lemma we know that given a spectrum $\hat{S}_j^{\mathcal{L}^2 opt}(\omega) \in \mathcal{L}^2[\Omega]$, there exist spectrum $\hat{S}_{nj}^{opt}(\omega) \in \Sigma_n[\Omega]$ for some $n \in \mathcal{N}$ such that:

$$\left| E(\{\hat{S}^{\mathcal{L}^2 opt}(\omega)\}) - E(\{\hat{S}_n^{opt}(\omega)\}) \right| < C(e) \tag{A.72}$$

or

$$-C(e) + E(\{\hat{S}^{\mathcal{L}^2 opt}(\omega)\}) < E(\{\hat{S}_n^{opt}(\omega)\}) < C(e) + E(\{\hat{S}^{\mathcal{L}^2 opt}(\omega)\}) \tag{A.73}$$

Since $C(e) = 2P\mu(S)[M^2 e + 2M\sqrt{\mu(\Omega)}]e$ we can choose e such that $C(e) < \delta$. Then based on (A.71) and (A.73) we will obtain:

$$E(\{\hat{S}_n^{opt}(\omega)\}) < E(\{\hat{S}^{opt}(\omega)\}) \tag{A.74}$$

with

$$\hat{S}_{nj}^{opt}(\omega) \in \Sigma_n[\Omega], \quad j = 1, ..., M \tag{A.75}$$

But this is a contradiction since we know that:

$$\min_{\hat{S}_{nj}(\omega) \in \Sigma_\infty[\Omega]} \left[E(\{\hat{S}_n(\omega)\}) \right] = E(\{\hat{S}^{opt}(\omega)\}) \quad \Sigma_n[\Omega] \subset \Sigma_\infty[\Omega] \quad \forall n \in \mathcal{N} \tag{A.76}$$

Therefore:

$$\min_{\hat{S}_j(\omega) \in \mathcal{L}^2[\Omega]} \left[E(\{\hat{S}(\omega)\}) \right] = E(\{\hat{S}^{opt}(\omega)\}) \tag{A.77}$$

A.4 Minimization of the quadratic form $E(\{S_i\})$

In this part of the appendix we specify the minimum of the following quadratic form:

$$E(\{S_i\}) = \{S_i\}^H[H_i]\{S_i\} + \{S_i\}^H\{l_i\} + \{S_i\}^H\{l_i\} + c_i \tag{A.78}$$

In order to convert the square error $E(\{S_i\})$ to a more familiar form we have to apply a technique similar to the "completing the squares" method. At this point we have to assume that the matrix $[H_i]$ is hermitian and positive definite. (The proof of this assumption is developed in section A.5). Under this assumption we can define the square root matrix of $[H_i]$ as a matrix $[K_i]$ such that:

$$[H_i] = [K_i]^H[K_i] \tag{A.79}$$

Also if we define vector $\{m_i\}$ as $\{m_i\} = [K_i^{-1}]^H\{l_i\}$ we have that:

$$\{l_i\} = [K_i]^H\{m_i\} \tag{A.80}$$

Finally based on (A.79) and (A.80), (A.78) becomes:

$$E = \{S_i\}^H[K]^H[K]\{S_i\} - \{S_i\}^H[K]^H\{m\} - \{m\}^H[K]\{f\} + c \tag{A.81}$$

By adding and subtracting the quantity $\{m_i\}^H\{m_i\}$ we obtain:

$$E = \{S_i\}^H [K_i]^H [K_i]\{S_i\} - \{S_i\}^H [K_i]^H \{m_i\} - \{m_i\}^H [K_i]\{S_i\} + \{m_i\}^H \{m_i\} + [c_i - \{m_i\}^H \{m_i\}] \tag{A.82}$$

or

$$E = \{[K_i]\{S_i\} - \{m_i\}\}^H \{[K_i]\{S_i\} - \{m_i\}\} + [c_i - \{m_i\}^H \{m_i\}] \tag{A.83}$$

Now it is easy to find the optimal vector $\{S_i\}^{opt}$ which minimizes E:

$$\{S_i\}^{opt} = [K_i^{-1}]\{m_i\} \quad \{S_i\}^{opt} = [K_i^{-1}][K_i^{-1}]^H \{l_i\} \tag{A.84}$$

Based on equation (A.79) it is true that $[K_i^{-1}][K_i^{-1}]^H [H_i] = [I]$ or $[K_i^{-1}][K_i^{-1}]^H = [H_i^{-1}]$. Therefore the optimal $\{S_i\}^{opt}$ becomes:

$$\{S_i\}^{opt} = [H_i^{-1}]\{l\} \tag{A.85}$$

Substituting back this optimal value to the initial expression of $E(\{S_i\})$ one has that:

$$\min [E(\{S_i\})] = c_i - \{l_i\}^H [H_i^{-1}]\{l_i\} \tag{A.86}$$

A.5 Hermitian and positive definite matrices $[H]$, $[H_i]$

In this section we show that if the wave sources are located in distinct points the matrices $[H(\omega)]$ and $[H_i]$ defined by:

$$
\begin{aligned}
&[H(\omega)]_{pq} = \int_S [G_p(\vec{r},\omega)G_q^*(\vec{r},\omega)]ds \\
&[H_i]_{pq} = \int_S \left[\int_{\Omega_i} G_p(\vec{r},\omega)G_q^*(\vec{r},\omega)d\omega\right] ds \\
&p,q \in \{1,...,M\} \;\; i \in \{1,...,2^n\}
\end{aligned} \tag{A.87}
$$

are hermitian and positive definite.

The fact that $[H(\omega)]$ is hermitian is trivial to show. In order to show that $[H(\omega)]$ is positive definite we have to look at the functions $G_j(\vec{r},\omega)$ which are continuous, non-zero and non-linear with respect to $\vec{r}$. Therefore each one of them cannot be written as a linear combination of the others.

$$
\sum_{j=1}^{M} \hat{f}_j(\omega)G_j(\vec{r},\omega) = 0 \Rightarrow \hat{f}_j(\omega) = 0 \;\; \forall j \in \{1,...,M\} \tag{A.88}
$$

Therefore, there exists a non-zero measure area $\delta S \in S$ such that:

$$
\forall \vec{r} \in \delta S \Rightarrow \left|\sum_{j=1}^{M} \hat{f}_j(\omega)G_j(\vec{r},\omega)\right| \neq 0 \quad \omega \in \Omega \tag{A.89}
$$

Therefore:

$$
\int_S \left|\sum_{j=1}^{M} \hat{f}_j(\omega)G_j(\vec{r},\omega)\right|^2 ds = \{\hat{f}(\omega)\}^H[H(\omega)]\{\hat{f}(\omega)\} > 0 \quad \forall\{\hat{f}(\omega)\} \neq \{0\}, \;\; \omega \in \Omega \tag{A.90}
$$

The last equation shows that the matrix [H] is positive definite. Based on the last equation it will be also true that:

$$\int_S \left[\int_{\Omega_i} \left| \sum_{j=1}^{M} f_{ij} G_j(\vec{r}, \omega) \right|^2 d\omega \right] ds = \{f_i\}^H [H_i] \{f_i\} > 0 \quad \forall \{f_i\} \neq \{0\}, \;\; \omega \in \Omega_i \;\; i \in \{1, ..., 2^n\} \tag{A.91}$$

The above proves that the matrix $[H_i]$ is also positive definite.

BIBLIOGRAPHY

[1] E. G. Williams: "Fourier Acoustics: Sound Radiation and Nearfield Acoustical Holography", *Academic Press, 1999*.

[2] C. H. Papas: "Theory of Electromagnetic wave propagation", *Dover Publications, October 1988*.

[3] A. Yariv, P. Yeh: "Optical Waves in Crystals: Propagation and Control of Laser Radiation", *Wiley, December 1983*.

[4] A. J. Berkhoot: "Applied Seismic Wave Theory", *Elsevier Publishing Company, October 1, 1987*.

[5] D. De Vries, E. W. Start, V. G. Valstar: "The Wave Field Synthesis Concept Applied to Sound Reinforcement: Restrictions and Solutions", 96^{th} *AES Convention, Amsterdam, February 26 March 01, 1994*.

[6] M. M. Boone: "Acoustic rendering with wave field synthesis", *ACM siggraph and eurographics campfire: Acoustic rendering for virtual environments, Snowbird Utah, May 26-29, 2001*.

[7] M. A. J. Baalman: "Application of Wave Field Synthesis in electronic music and sound installations", *Linux Audio Conference, 29 April - 2 May 2004, ZKM Karlsruhe, Germany*.

[8] J. S. Tan, L. A. Frizzell, N. Sanghvi, S. Wu, R. Seip, J. T. Kouzmanoff: "Ultrasound phased arrays for prostate treatment", *J. Acoust. Soc. Am. 109 (6), pp. 3055-3064, June 2001*.

[9] O. M. Al-Bataineh, N. B. Smith, R. M. Keolian V. W. Sparrow, L. E. Harpster: "Optimized hyperthermia treatment of prostate cancer using a novel intracavitary ultrasound array", *J. Acoust. Soc. Am. 114, pp. 2347, 2003*.

[10] M. Tanter, J. F. Aubry, J. Gerber, J. L. Thomas, M.Fink: "Optimal focusing by spatio-temporal inverse filter. I. Basic Principles", *J. Acoust. Soc. Am. 110(1), pp. 37-47, July 2001*.

[11] R. Piestun, B. Spector, J. Shamir: "Wave fields in three dimensions: Analysis and Synthesis", *J. Opt. Soc. Amer. A., Vol. 13, No. 9, pp. 1837 - 1848, September 1996*.

[12] R. Piestun, J. Shamir, "Synthesis of Three Dimensional Light Fields and Applications", *Proc. IEEE, Vol. 90, No. 2, pp. 222-244, February 2002*.

[13] R. S. Pellegrini, M. Rosenthal: "Wave Field Synthesis with synchronous distributed signal processing", *IEEE 6th Workshop on Multimedia Signal Processing 2004*.

[14] S. Spors, H. Buchner, R. Rabenstein: "A novel approach to active listening room compensation for wave field synthesis using wave-domain adaptive filtering", *IEEE International Conference on acoustics, speech and signal processing 2004*.

[15] P. Gauthier, A. Berry: "Adaptive wave field synthesis with independent radiation mode control for active sound field reproduction: Theory", *J. Acoust. Soc. Am., Vol. 119, No. 6, pp. 2721-2737, May 2006*.

[16] P. Gauthier, A. Berry: "Adaptive wave field synthesis for active sound field reproduction", *J. Acoust. Soc. Am., Vol. 123, No. 5, pp. 1991-2016, April 2008*.

[17] T. D. Mast, W. Faidi, I. R. S. Makin: "Acoustic field modeling in therepeutic ultrasound", 17th *International Symposium on Nonlinear Acoustics, State College PA, July 2005*.

[18] O. C. Zienkiewicz: "The Finite Element Method", *Mc Graw Hill, 1989*.

[19] G. N. Lilis, A. Halder, S. Telukunta, S. Servetto: "Hybrid numerical Scheme for time-evolving wave fields", *International Journal for Numerical methods in Engineering, Vol. 71, 3, pp. 277-312, November 2006*.

[20] M. Camras: "Approach to recreating a sound field", *The Journal of the Acoustical Society of America, Vol. 43, No. 6, pp. 1425-1431, June 1968*.

[21] A. J. Berkhout: "A Holographic Approach to Acoustic Control", *The Journ. Audio Eng. Soc., Vol. 36, Issue 12, pp. 977-995, December 1988*.

[22] A. J. Berkhout, D.De Vries, P. Vogel: "Acoustic Control by Wave Field Synthesis", *The Journal of the Acoustical Society of America, Vol. 93, Issue 5, pp. 2764-2778, May 1993*.

[23] A. J. Berkhout, D. de Vries, J. J. Sonke: "Array technology for acoustic wave field synthesis in enclosures", *The Journal of the Acoustical Society of America, Vol. 102, pp. 2757-2770, 1997*.

[24] E. Wolf: "The life and work of Christiaan Huygens", *Huygens' principle 1690-1990 : theory and applications, Amsterdam, 1992*.

[25] M. M. Boone, E. N. G. Verheijen, P. F. Van Tol: "Spatial sound field reproduction by wave field synthesis", *J. Audio Eng. Soc., Vol. 43, 12, pp. 1003 - 1012, 1995*.

[26] R. Rabenstein, S. Spors: "Spatial sound reproduction with wave field synthesis", *AES Italian Section, Como, November 2-5, 2005*.

[27] K. Brandenburg, S. Brix, T. Sporer: "Wave Field Synthesis: From research to applications", *XII European Signal Processing Conference 2004, September 6-10, Vienna, Austria*.

[28] J. Escolano, S. Bleda, B. Pueo, J. J. Lopez: "Wave field synthesis simulation by means of finite-difference time-domain technique", *XII European Signal Processing Conference 2004 september 6-10 2004 Vienna, Austria*.

[29] E. Corteel: "Synthesis of Directional Sources Using Wave Field Sythesis, Posibilities and Limitations", *EURASIP Journal on Advances in Signal Processing*.

[30] H. L. Royden: "Real Analysis", *Third edition, Macmillan publishing co NY, 1988*.

[31] D. H. Griffel: "Applied Functional Analysis", *Dover Publications, Jun 14, 2002*.

[32] A. Sommerfeld: "Partial Differential Equations", *Academic Press, 1949*.

[33] R. C. Aster, B. Borchers, C. H. Thurber: "Parameter Estimation and Inverse Problems", *Elsevier academic press, 2005*.

[34] P. M. Woodward, J. D. Lawson: "The theoretical precision with which an arbitrary radiation pattern may be obtained from a source of finite size", *J.IEE (London), pt. III, Vol. 95, pp. 363-370, September 1948*.

[35] D. R. Rhodes: "The Optimum Line Source for the Best Mean-Square Approximation to a Given Radiation Pattern", *IEEE Trans. Antennas and Propag., Vol. AP-11, pp. 440-446, July 1963*.

[36] G. Deschamps, H. S. Cabayan: "Antenna Synthesis and Solution of Inverse Problems by Regularization Methods", *IEEE Trans. Antennas and Propag., Vol. AP-20, No. 3, pp. 268-274, May 1972*.

[37] J. R. Mautz, R. F. Harrington: "Computational Methods for Antenna Pattern Synthesis", *IEEE Trans. Antennas and Propag., Succint Papers, pp. 507-512, July 1975*.

[38] H. Chang, T. K. Sarkar, O. M. C. Pereira-Filho: "Antenna Pattern Synthesis Utilizing Spherical Bessel Functions", *IEEE Trans. Antennas and Propag., Vol. 48, No. 6, pp. 853-859, June 2000*.

[39] R. J. Mailloux: *Phased Array Antenna Handbook Norwood, MA: Artech House 1994*.

[40] D. Parker, D. Zimmermann: "Phased Arrays - PartI: Theory and Architectures", *IEEE Trans. Microw. Theory Tech., Vol. 50, No. 3, pp. 678-686, March 2002*.

[41] W. H. Von Aulock: "Properties of Phased Arrays", *Proc. IRE, pp. 1715-1727, 1960*.

[42] J. Colin: "Phased array radars in France: Present and future", *IEEE Int. Phased Array Syst. Technol. Symp. Dig., pp. 458-459, October 1996*.

[43] B. Smolders, G. Hampson: "Deterministic RF Nulling in Phased Arrays for the Next Generation of Radio Telescopes", *IEEE Antennas and Propagat. Mag., Vol. 44, No. 4, pp. 13-22, August 2002*.

[44] A. Hajimiri, H. Hashemi, A. Natarajan, X. Guan, A. Komijani: "Integrated Phased Array Systems in Silicon", *Proc. IEEE, Vol. 93, No. 9, pp. 1637-1655, September 2005*.

[45] A. Natarajan, A. Komijani, A. Hajimiri: "A fully integrated 24-GHz Phased-Array Trnasmitter in CMOS", *IEEE J. Solid-State Circuits, Vol. 40, No. 12, pp. 2502-2514, December 2005*.

[46] L. D. Di Domenico, G. M. Rebeiz: "Digital Communications Using Self-Phased Arrays", *IEEE Trans. Microw. Theory Tech., Vol. 49, No. 4, pp. 677-684, April 2001*.

[47] J. Roderick, H. Krishnaswamy, K. Newton, H. Hashemi: "Silicon-Based Ultra-Wideband Beam-Forming", *IEEE J. Solid-State Circuits, Vol. 41, No. 8, pp. 1726-1739, August 2006*.

[48] G. Michel, M. Thumm: "Field profile synthesis with an antenna array", *Int. J. Infrared and Milimiter Waves, Vol. 19, No. 3, pp. 419-426, 1998*.

[49] M. S. Narasimhan, K. Varadarangan, S. Christopher: "A new thechnique of Synthesis of the near or Far-Field Patterns of Arrays", *IEEE Trans. Antennas and Propag., Vol. AP-34, No. 6, pp. 773-778, June 1986*.

[50] K. Soetanto, H. Watarai: "Development of magnetic Microbubbles for Drug Delivery System (DDS)", *Jpn. J. Appl. Phys., Vol. 39, pp. 3230 - 3232, May 2000*.

[51] D. A. Kharkevich, R. N. Alyautdin, V. I. Filippov, A. Yu. Nemirovskii, S. A. Kasparov, A. A. Kuznetsov: "Experimental study of magnetically controlled transport of neuromuscular blocking agents diadonium and dipyronium in animals", *Bulletin of Experimental Biology and Medicine, Vol. 102, No. 1, pp. 926-928, July 1986*.

[52] A. Roger: "Newton-Kantorovitch Algorithm Applied to an Electromagnetic Inverse Problem", *IEEE Trans. Antennas and Propag., Vol. AP-29, No. 2, pp. 232-238, March 1981*.

[53] A. Qing: "Electromagnetic Imaging of Two-Dimensional Perfectly Conducting Cylinders With Transverse Electric Scattered Field", *IEEE Trans. Antennas and Propag., Vol. 50, No. 12, pp. 1786-1794, December 2002*.

[54] W. Rieger, M. Haas, C. Huber, G. Lehner, W. M. Rucker: "Image Reconstruction from Real Scattering Data Using an Iterative Scheme with Incorporated a priori Information", *IEEE Antennas and Propagat. Mag., Vol. 41, No. 2, pp. 33-40, April 1999*.

[55] A. J. Peyton, Z. Z. Yu, S. Al-Zeibak, N. H. Saunders, A. R. Borges: "Electromagnetic Imaging Using Mutual inductance Tomography: Potential for Process Applications", *Particle and Particle Systems Characterization, Vol. 12, Issue 2, pp. 68-74, 1995*.

[56] M. Terada: "Distance-Selective Wireless Networks with Enhanced Isolation Characteristics: A New Concept Based on Three-Dimensional Wave Field Synthesis for Volumetric-Controlled Field Coverage", *Antennas and Propag. Soc. Int. Symp., 2004 IEEE, Vol. 2, 20-25, pp. 1736 - 1739, June 2004*.

[57] L. Brillouin: "Wave Propagation in Periodic Structrures: Electric filters and Crystal Lattices", *Dover Publications, 1953*.

[58] T. W. Crowe, W. L. Bishop, D. W. Porterfield, J. L. Hesler, R. M. Weikle: "Opening the Terahertz Window With Integrated Diode Circuits", *IEEE Journ. of solid-state circuits, Vol. 40, No. 10, October 2005*.

[59] J. C. Eilbeck, P. S. Lomdahl, A. C. Newell: "Chaos in the inhomogeneously driven sine-Gordon equation", *Phys. Lett. 87A, pp. 1-4, 1981*.

[60] A. R. Bishop, P. S. Lombdahl: "Nonlinear Dynamics in driven, damped sine-gordon systems", *Physica D, Vol 18, 1-3, pp. 54-66, January 1986*.

[61] S. Watanabe, S. J. Herre, Van Der Znat, S. H. Strogatz, T. P. Orlando: "Dynamics of circular arrays of Josephson junctions and the discrete sine-Gordon equation", *Physica D, Vol. 97, pp. 429-470, 1996*.

[62] M. Feckan, V. M. Rothos: "Travelling waves in Hamiltonian systems on 2D Lattices with nearest neighbor interactions", *Nonlinearity, Vol. 20, pp. 319-341, 2007*.

[63] J. L. Marin, S. Aubry: "Breathers in nonlinear lattices: numerical calculation from the anticontinuous limit", *Nonlinearity 9, pp. 1501-1528, 1996*.

[64] P. S. Lomdahl, M. R. Samuelsen: "Persistent breather excitations in an ac-driven sine-Gordon system with loss", *Phys. Rev. A, Vol. 34, No. 1, pp. 664-667, July 1986*.

[65] I. A. Butt, J. A. D. Wattis: "Discrete breathers in a two-dimensional Fermi-Past-Ulam lattice", *J. Phys. A: Math. Gen., Vol. 39, pp. 4955-4984, 2006*.

[66] I. A. Butt, J. A. D. Wattis: "Discrete breathers in a two-dimensional hexagonal Fermi-Past-Ulam lattice", *J. Phys. A: Math. Theor., Vol. 40, pp. 1239-1264, 2007*.

[67] B. A. Malomed: "Damping and pumping of localized intrinsic modes in nonlinear dynamical lattices", *Phys. Rev. B, Vol. 49, No. 9, March 1994*.

[68] A. Vanossi, K. O. Rasmussen, A. R. Bishop, B. A. Malomed, V. Bartolani: "Spontaneous pattern formation in driven nonlinear lattices", *Phys. Rev. E, Vol. 62, pp.7353, April 2000*.

[69] H. S. Bhat, E. Afshari: "Nonlinear constructive interference in electrical lattices", *Phys. Rev. E, Vol. 77, No. 6, June 2008*.

[70] R. Landauer: "Shock Waves in Nonlinear Transmission Lines and Their Effect on Parametric Amplification", *IBM J. Res. Develop. 4, pp. 391-401 (1960)*.

[71] R. Hirota, K. Suzuki: "Studies on Lattice Solitons by Using Electrical Networks", *J. Phys. Soc. Japan 28, pp. 1366-1367 (1970)*.

[72] H. Ikezi, S. S. Wojtowicz, R. E. Waltz, D. R. Baker: "Temporal contraction of solitons in a nonuniform transmission line", *J. Appl. Phys., Vol. 64, No. 12, pp. 6836-6838, 1988*.

[73] M. Case, M. Kamegawa, R. Yu, M. J. W. Rodwell, J. Franklin: "Impulse compression using soliton effects in a monolithic GaAs circuit", *Appl. Phys. Lett., Vol. 58, No. 2, pp. 173175, January 14, 1991*.

[74] M. Case, E. Carman, R. Yu, M. J. W. Rodwell: "Picosecond Duration, Large-Amplitude Impulse Generation Using Electrical Soliton Effects", *Applied Physics Letters, Vol. 60, No. 24, pp. 3019-3021, June 15, 1992*.

[75] E. Afshari, A. Hajimiri: "A Non-Linear Transmission Lines for Pulse Shaping in Silicon", *Custom Integrated Circuits Conference, San Jose, pp. 91-94, September 2003*.

[76] E. Afshari, H. S. Bhat, A. Hajimiri: "Solitonic Pulse Shaping on Silicon", *Submission for Stanford-Berkeley-Caltech Innovators Challenge, April 2005*.

[77] E.Afshari, H. S. Bhat, A. Hajimiri, J. E. Marsden: "Extremely Wideband Signal Shaping using One and Two Dimensional Non-Uniform Nonlinear Transmission Lines", *Journal of Applied Physics, Volume 99, Issue 5, March 2006*.

[78] L. A. Ostroviskii, V.V.Papko, Y.A.Stepanyants: "Solitons and nonlinear resonance in two-dimensional lattices", *Sov. Phys. JETP, Vol 51, No. 2, February 1980*.

[79] Y. A. Stepanyants: "Experiemtnal study of "Cerenkov" radiation form solitons in two dimensional LC-Lattices", *Radiophysics and Quantum Electronics, Vol. 26, No. 7, pp. 601-607, July 1983*.